

# Polarimetric MIMO arrays for automotive radar

Preliminary literature review report

23<sup>RD</sup> JANUARY, 2026

MARTIN ŠIMÁK

---

## Abstract

The goal of this document is to present a preliminary literature review report, summarizing roughly the first months of research and consisting of an initial dive into the state of the art in the area of polarimetric MIMO radar for automotive applications in search for deep insights and directions of further advancements.

---

<b>1</b>	<b>Introduction</b>	<b>2</b>
<b>2</b>	<b>Radar polarimetry</b>	<b>4</b>
<b>3</b>	<b>Front-end technologies</b>	<b>15</b>
<b>4</b>	<b>MIMO array design</b>	<b>22</b>

# Chapter 1

## Introduction

Automotive radar is a rapidly-evolving field of research, driven by the increasing demand for enhanced driver safety and the eventual realization of autonomous vehicles [1]. While the initial vision of fully autonomous driving has faced regulatory and technological hurdles, the major focus of the industry has pragmatically shifted. The immediate goal is now the improvement of driver safety through advanced driver-assistance systems (ADAS). This forms a crucial foundational step, with the progressive automation of further features over time being the pathway towards full vehicle autonomy.

Modern ADAS increasingly rely on robust environmental perception to ensure safety and reliable operation across a wide range of road conditions. Among all sensing modalities, millimetre-wave radar at 77–81 GHz remains uniquely resilient to adverse weather, low visibility, and non-cooperative targets. While contemporary automotive radars provide accurate range, velocity and angular estimates, their classification capability remains fundamentally limited. Radar systems in vehicles are predominantly single-polarized MIMO arrays, optimized for geometric detection but not for detailed scattering characterization. As a result, the ability to distinguish vulnerable road users (VRUs) – including pedestrians, cyclists, and scooter riders – from background clutter or other vehicles is still insufficient for high-level scene understanding [2].

In contrast, radar polarimetry has long demonstrated powerful discrimination capabilities in other domains such as remote sensing, weather radar, and synthetic aperture radar (SAR). Polarimetric measurements capture how objects transform the polarization state of the incident electromagnetic field, thereby revealing structural, material and orientation-dependent scattering properties. These additional degrees of freedom can support classification tasks that are fundamentally unattainable with intensity-only radar data. Yet, despite its maturity in other fields, polarimetry has not been adopted in commercial automotive radar. Early research prototypes indicate its potential, but the fundamental theoretical, technological and calibration challenges remain unresolved.

Furthermore, the transition to high-resolution 2D MIMO arrays in automotive radars introduces new opportunities for capturing polarization-diverse scattering. Larger virtual apertures, wide angular fields of view and sparse array concepts can benefit polarimetric imaging – but they also exacerbate issues such as cross-polar coupling, mutual coupling between antennas, phase-centre misalignment and channel imbalance. These limitations motivate a systematic reassessment of array topologies, antenna technologies, and processing schemes required for polarimetric MIMO radar at W-band.

This literature review therefore aims to synthesize the state of the art in:

- radar polarimetry theory and its applicability to automotive environments,
- antenna technologies suitable for dual-polarization operation at 77–81 GHz,
- MIMO array topologies and multiplexing schemes relevant for polarimetric systems, and

- signal-processing and calibration methods required for polarimetric reconstruction.

The synthesis identifies critical gaps in current knowledge – most notably the lack of a polarimetric method suitable for dynamic road scenes, Doppler-resolved polarimetry at mmWave, and MIMO array designs optimized jointly for polarization purity and automotive integration. These insights form the basis for the research contributions of this PhD: the development of a new polarimetric method for automotive radar, the design of a polarimetric MIMO array demonstrator, and the establishment of a dedicated measurement experiment for extracting target polarimetric signatures.

# Chapter 2

## Radar polarimetry

Although the foundational ideas of radar polarimetry date back to the 1970s and can be considered a mature concept – with the 1980s and 1990s representing a golden period of theoretical and experimental development for SAR and meteorology [3] – its application potential in the automotive industry began to emerge only in the previous decade. In remote sensing, polarimetry has long been the standard for classifying terrain textures or hydrometeor shapes; however, transferring these techniques to the automotive domain presents unique challenges. Unlike the far-field, high-altitude geometries of SAR, automotive radar operates at grazing incidence angles with significant multipath interaction, in the near-to-intermediate field, and against highly dynamic, non-cooperative targets.

Consequently, the field of polarimetric automotive radar remains in its infancy, lacking robust methods for classifying dynamic VRUs such as pedestrians and cyclists. Nonetheless, it holds a compelling promise for achieving higher reliability and sophistication in sensors for ADAS and autonomous driving. This promise has captured the attention of major automotive companies and research institutes, prompting viability confirmations [2] and proof-of-concept system implementations [4]. The rapidly increasing innovation in this area is further evidenced by the recent emergence of monographs focusing specifically on polarimetric radar for automotive applications [5].

Establishing a polarimetric framework for VRU classification, however, places stringent demands on the underlying radar architecture. The theoretical requirements for high polarization purity and cross-polarization discrimination (XPD) directly inform the selection of radiating element types and feeding integration platforms, as will be discussed in detail in Chapter 3. Furthermore, the need for simultaneous acquisition of the full scattering matrix for dynamic scenes necessitates a sophisticated large-aperture MIMO configuration. The design of this MIMO topology and its impact on virtual aperture and polarimetric diversity will be the focus of Chapter 4. This introductory chapter therefore provides the theoretical and phenomenological motivation for the hardware and topological developments that follow.

The exposition given in this chapter follows standard references to electrodynamics and radar polarimetry, such as Zangwill [6] and Lee and Pottier [3]. Additionally, a specialized monograph on polarimetric radar for automotive applications by Visentin [5], is discussed to provide further context and detail.

### 2.1 Fundamentals of radar polarimetry

Electromagnetic waves can be decomposed into orthogonal linear, circular, or elliptical polarization states, each associated with a specific temporal evolution of the electric field vector. In radar applications, polarization serves as an additional dimension for characterizing scattering mechanisms: targets may preserve, transform, or depolarize the incident wave depending on their geometry, surface material, roughness, and orientation. These transformations provide valuable

Add citations through-out the chapter.

classification features that are absent in scalar radar measurements [3].

The description of polarization typically relies on the Jones vector for coherent fields and the Stokes vector or coherency matrix for partially coherent and incoherent fields. At automotive millimetre-wave frequencies, the high coherence of FMCW radars allows Jones and coherency representations to remain applicable. The polarization purity of the transmitted and received waves, however, is strongly influenced by antenna cross-polarization discrimination (XPD), PCB anisotropies, and mutual coupling – highlighting the need for the careful array design discussed in Chapter 3.

**Time convention.** As common in engineering monographs, this text treats the convention of time as *positive*, meaning that a scalar wave  $w(\xi, t)$  propagating in the  $\xi$  direction is expressed as  $\exp[i(\omega t - k\xi)]$ . This is in contrast to physics literature, which often adopts a *negative time* convention, leading to  $\exp[i(k\xi - \omega t)]$ .

### 2.1.1 Polarization of electromagnetic waves

While the full propagation of electromagnetic energy is governed by Maxwell's equations, for radar polarimetry it suffices to consider the solution for a monochromatic plane wave propagating in a direction given by the wave vector  $\mathbf{k} = k\mathbf{e}_k$  with angular frequency  $\omega = 2\pi f$ . Such electric and magnetic vector fields can be expressed as

$$\mathbf{E}(\mathbf{r}, t) = \mathcal{E}_{\perp} \exp[i(\omega t - \mathbf{k} \cdot \mathbf{r})] \quad \text{and} \quad \mathbf{B}(\mathbf{r}, t) = \mathcal{B}_{\perp} \exp[i(\omega t - \mathbf{k} \cdot \mathbf{r})], \quad (2.1)$$

where  $\mathcal{E}_{\perp}$  and  $c\mathcal{B}_{\perp} = \mathbf{e}_k \times \mathcal{E}_{\perp}$  are generally complex amplitude vectors perpendicular to the direction of propagation. The physical fields of a monochromatic plane wave are the *real parts* of these expressions. Focusing on the electric field component, we have

$$\mathbf{E}(\mathbf{r}, t) = \begin{bmatrix} |E_H| \exp(i\delta_H) \\ |E_V| \exp(i\delta_V) \end{bmatrix} \exp[i(\omega t - kz)], \quad (2.2)$$

where  $\delta_H$  and  $\delta_V$  denote the phase offsets of the horizontal and vertical components, respectively. The choice of the transverse basis vectors is arbitrary; however, in radar applications, it is customary to select orthogonal basis vectors perpendicular to the direction of propagation, horizontal ( $H$ ) and vertical ( $V$ ).

The polarization state – the geometric locus traced by the tip of the electric field vector over time – is fully described by the Jones vector  $\mathbf{E}_J$ . For a fully coherent wave, the *Jones vector* is defined by the amplitudes  $|E_H|$  and  $|E_V|$  and the relative phase difference  $\delta = \delta_V - \delta_H$ :

$$\mathbf{E}_J = \begin{bmatrix} E_H \\ E_V \end{bmatrix} = \begin{bmatrix} |E_H| e^{i\delta_H} \\ |E_V| e^{i\delta_V} \end{bmatrix} = e^{i\delta_H} \begin{bmatrix} |E_H| \\ |E_V| e^{i\delta} \end{bmatrix}. \quad (2.3)$$

This representation is critical for the MIMO system design discussed in Chapter 4, as the transmitter and receiver chains operate coherently. However, the Jones vector is strictly valid only for fully polarized, monochromatic waves.

### 2.1.2 The Sinclair scattering matrix

When concerned with scattering off targets, the relationship between the incident and scattered electric fields is of primary interest. As discussed in the previous sections, polarization of a monochromatic plane wave at a given instant can be fully characterized by the Jones vector. Furthermore, a set of two orthogonal Jones vectors forms a polarization basis. Therefore, it is possible to establish a linear scattering model that relates the incident and scattered Jones vectors,  $\mathbf{E}_{\text{in}}$  and  $\mathbf{E}_{\text{sc}}$ , respectively, via a complex scattering matrix:

$$\mathbf{E}_{\text{sc}} = \frac{e^{-ikr}}{r} \mathbf{S} \mathbf{E}_{\text{in}} = \frac{e^{-ikr}}{r} \begin{bmatrix} S_{HH} & S_{HV} \\ S_{VH} & S_{VV} \end{bmatrix} \mathbf{E}_{\text{in}}. \quad (2.4)$$

The matrix  $\mathbf{S}$ , called the *Sinclair scattering matrix*, encapsulates the target's polarimetric response, with each element  $S_{pq}$  representing the complex scattering amplitude from transmit polarization  $p$  to receive polarization  $q$ . The diagonal terms are often called *co-polar* components, while the off-diagonal terms are referred to as *cross-polar* components. Furthermore, under the assumption of reciprocity in a linear, time-invariant medium, the scattering matrix is symmetric, yielding

$$\mathbf{S} = \exp(i\phi_{HH}) \begin{bmatrix} |S_{HH}| & |S_{HV}| \exp[i(\phi_{HV} - \phi_{HH})] \\ |S_{HV}| \exp[i(\phi_{HV} - \phi_{HH})] & |S_{VV}| \exp[i(\phi_{VV} - \phi_{HH})] \end{bmatrix}. \quad (2.5)$$

The absolute phase term  $\exp(i\phi_{HH})$  is not considered an independent parameter since it represents an arbitrary value given by the target range. The main consequence of this symmetry is a reduction in the number of independent parameters from eight to five.<sup>1</sup> However, practical considerations in automotive radar often challenge this ideal model by introducing near-field effects: Reciprocity holds for plane waves; for targets in the near-field of the array, such as a pedestrian situated 2 m away from the antenna, the wavefront curvature may introduce deviations.

**Scattering coordinate frameworks.** When defining the polarimetric scattering matrix, it is necessary to assume a frame in which the polarization is defined. Generally, there are two principal conventions: the *forward scatterer alignment* (FSA) and the *backscatterer alignment* (BSA). While the FSA convention, sometimes called *wave-oriented*, defines the polarization basis for both incident and scattered waves so that the Cartesian  $z$ -axis always faces the  $\mathbf{k}$  direction, the BSA system operates by defining the basis of the scattered wave with respect to the receiving antenna. This text assumes the BSA convention, as is standard for monostatic radar. This choice simplifies the scattering definition by defining a fixed coordinate system for both the incident and backscattered waves relative to the antenna.

**From theoretical scattering to observed signatures.** While the Sinclair matrix  $\mathbf{S}$  provides a deterministic description of target scattering in an ideal environment, the transition to practical automotive sensing introduces two significant layers of complexity: hardware-induced distortion and the stochastic nature of distributed targets.

In practical scenarios, the measured matrix  $\mathbf{M}$  is a transformation of the true scattering matrix  $\mathbf{S}$  through the system's transfer functions. This is typically modelled as<sup>2</sup>

$$\mathbf{M} = \mathbf{RST} + \mathbf{C} + \mathbf{N}, \quad (2.6)$$

where  $\mathbf{T}$  and  $\mathbf{R}$  represent the polarimetric imbalances of the transmitter and receiver chains,  $\mathbf{C}$  accounts for antenna mutual coupling and leakage, and  $\mathbf{N}$  is the additive noise. Characterizing these terms is the primary objective of the calibration routines detailed in ??.

Second, in the presence of complex, non-point-like targets such as VRUs, a single Sinclair matrix is often insufficient to capture the depolarization caused by multiple scattering centres. This necessitates the use of the second-order statistics introduced in the following section.

### 2.1.3 Stokes parameters and the Poincaré sphere

In dynamic automotive scenarios, electromagnetic waves typically interact with *distributed scatterers* – extended targets such as road surfaces, vegetation, vehicles, or tunnel walls that

---

<sup>1</sup>Even after this reduction, fully polarimetric systems, capable of measuring the full scattering response, dispose of five independent parameters per resolution cell. This is in contrast to single-polarized systems, which measure only two, and it shows the increased complexity and information content of polarimetric measurements.

<sup>2</sup>In polarimetric calibration, the equation is commonly expressed ‘backwards’, that is, by equating the ideal scattering matrix to the measured one transformed by  $\mathbf{R}$  and  $\mathbf{T}$  as the *correction* matrices. Here, we express it in the *forward* direction to emphasize the measurement process, hence taking  $\mathbf{R}$  and  $\mathbf{T}$  as the *distortion* matrices.

comprise numerous independent scattering centres within a single resolution cell. Because these sub-reflectors contribute random phase and amplitude fluctuations, the resulting interference induces depolarization, rendering the reflected wave partially polarized or incoherent. To characterize these complex fields, the Stokes parameters are employed; they provide a phase-agnostic description of the wave's polarization state based on observable, time-averaged power measurements.

The transition from Jones formalism to Stokes parameters involves considering the Jones vector components as random processes,  $E_H(t)$  and  $E_V(t)$ . Taking the time-averaged<sup>3</sup> outer product of the Jones vector yields the Hermitian positive semidefinite wave covariance matrix  $\mathbf{J}$ , often called the *coherency matrix*:

$$\mathbf{J} = \langle \mathbf{E}_J \cdot \mathbf{E}_J^\dagger \rangle = \begin{bmatrix} \langle |E_H|^2 \rangle & \langle E_H E_V^* \rangle \\ \langle E_V E_H^* \rangle & \langle |E_V|^2 \rangle \end{bmatrix}, \quad (2.7)$$

where  $\langle \cdot \rangle$  denotes temporal averaging. To facilitate convenient description through matrix decomposition, group theory is often employed. Specifically, the formalism considers the SU(2) group basis consisting of the Pauli matrices:

$$\boldsymbol{\sigma}_0 = \begin{bmatrix} 1 & 0 \\ 0 & 1 \end{bmatrix}, \quad \boldsymbol{\sigma}_1 = \begin{bmatrix} 1 & 0 \\ 0 & -1 \end{bmatrix}, \quad \boldsymbol{\sigma}_2 = \begin{bmatrix} 0 & 1 \\ 1 & 0 \end{bmatrix}, \quad \boldsymbol{\sigma}_3 = \begin{bmatrix} 0 & -i \\ i & 0 \end{bmatrix}. \quad (2.8)$$

These matrices form a basis for decomposing the coherency matrix – a decomposition technique commonly known as the *Pauli decomposition*:

$$\mathbf{J} = \frac{1}{2} \sum_{i=0}^3 g_i \boldsymbol{\sigma}_i = \frac{1}{2} \begin{bmatrix} g_0 + g_1 & g_2 - ig_3 \\ g_2 + ig_3 & g_0 - g_1 \end{bmatrix}. \quad (2.9)$$

Here, the coefficients  $g_i$  are the *Stokes parameters*, defined as  $g_i = \text{tr}(\mathbf{J} \boldsymbol{\sigma}_i)$ . Together, they form the *Stokes vector*  $\mathbf{g}$ , expressed as

$$\mathbf{g} = \begin{bmatrix} g_0 \\ g_1 \\ g_2 \\ g_3 \end{bmatrix} = \begin{bmatrix} \langle |E_H|^2 \rangle + \langle |E_V|^2 \rangle \\ \langle |E_H|^2 \rangle - \langle |E_V|^2 \rangle \\ 2 \operatorname{Re} \langle E_H E_V^* \rangle \\ -2 \operatorname{Im} \langle E_H E_V^* \rangle \end{bmatrix}. \quad (2.10)$$

As evident from Equation (2.10), the Stokes parameters are *real-valued power quantities* directly measurable via standard RF detectors. While the diagonal elements  $J_{pq}$  represent the intensities, the off-diagonal elements capture the complex cross-correlation between the horizontal and vertical components. Geometrically, the parameters  $g_1, g_2, g_3$  span a three-dimensional orthogonal basis, mapping the polarization state onto the *Poincaré sphere*, as illustrated in Figure 2.1. Within this topological framework, the parameter  $g_0$  represents the total wave intensity and corresponds to the radius of the sphere.

Consequently, the condition of physical realizability – derived from the positive semidefiniteness of the coherency matrix – requires that the state vector lies either on the surface or within the volume of the sphere:

$$g_0^2 \geq g_1^2 + g_2^2 + g_3^2. \quad (2.11)$$

The equality in Equation (2.11) holds strictly for fully polarized waves, which map to the sphere's surface. Conversely, the strict inequality characterizes partially polarized waves, which occupy the interior volume and are typical of clutter and distributed targets. This geometric distinction

---

<sup>3</sup>Taking the outer product of a single Jones vector  $\mathbf{E}_J = [E_H, E_V]^T$  without averaging would yield a rank-1 matrix, corresponding to the theoretical ideal of a fully polarized, perfectly coherent wave. Temporal averaging is essential to capture partial polarization effects.

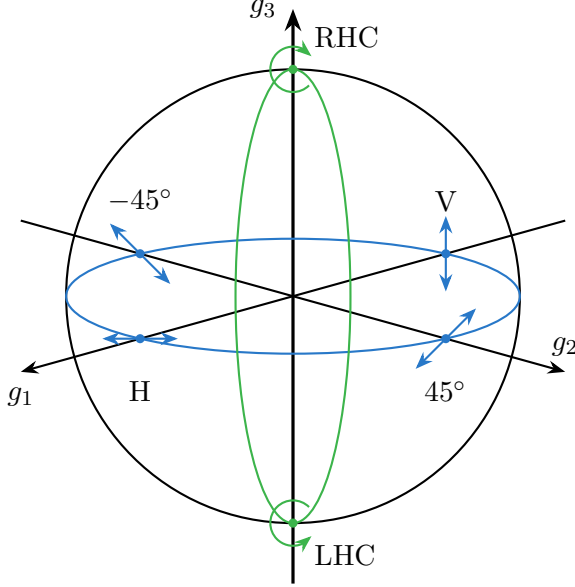


Figure 2.1: Representation of the polarization state on the Poincaré sphere. Fully polarized waves lie on the surface ( $DOP = 1$ ), while partially polarized states lie within the volume ( $DOP < 1$ ). The axes  $g_1, g_2, g_3$  correspond to linear, linear-diagonal, and circular polarizations, respectively.

naturally leads to the definition of the *degree of polarization* (DOP) as the normalized radial distance from the origin:

$$DOP = \frac{\sqrt{g_1^2 + g_2^2 + g_3^2}}{g_0} = \sqrt{1 - 4 \frac{\det(\mathbf{J})}{\text{tr}(\mathbf{J})^2}}. \quad (2.12)$$

This metric serves as a key discriminant between stable VRU scatterers and distributed clutter, a feature that will be exploited in later chapters ?? for target classification. By applying *polarimetric decompositions* to the coherency matrix  $\mathbf{J}$ , we can decouple the scattering into constituent mechanisms, such as single-bounce, double-bounce, and volume scattering. In the following sections, these decomposition theorems are utilized to extract robust polarimetric signatures, providing the feature set required for the classification models developed later in this work.

## 2.2 Polarimetric target decomposition

The Sinclair and coherency matrices derived in Section 2.1 contain the complete polarimetric information of a target. However, in their raw matrix form, they offer little direct insight into the physical geometry of the scatterer. *Target decomposition* theorems aim to invert this relationship, expressing the measured matrix as a linear combination of canonical scattering mechanisms – such as flat plates, dihedrals, or dipoles – thereby extracting semantic features for classification.

These methods are broadly categorized into *coherent decompositions*, which operate on the Sinclair scattering matrix of deterministic targets, and *incoherent decompositions*, which operate on the second-order statistics of distributed targets.

### 2.2.1 Coherent decomposition

For deterministic targets with negligible noise and spatial variation, such as a car chassis or a corner reflector, the scattering process is fully coherent. As described by Gaglione et al. [7],

a general coherent polarimetric decomposition of the Sinclair matrix  $\mathbf{S}$  can be expressed as a linear combination of  $M$  elementary scattering mechanisms; that is,

$$\mathbf{S} = \sum_{m=1}^M c_m \mathbf{S}_m, \quad (2.13)$$

where  $\mathbf{S}_m$  are the canonical scattering matrices, encoding the response of the  $m$ -th canonical object, and  $c_m$  are generally complex coefficients, including both amplitude and phase information of each scattering mechanism.

The most established framework for interpreting radar targets is the *Pauli decomposition*, which projects the Sinclair matrix onto a scaled basis of Pauli matrices,  $\{\sqrt{2}\boldsymbol{\sigma}_i\}_{i=0}^3$ , where  $\boldsymbol{\sigma}_i$  are defined in Equation (2.8).<sup>4</sup> The resulting vector representation of the scattering matrix,  $\mathbf{S}$ , is referred to as the *Pauli scattering vector*, defined as

Add a section on canonical scatterers prior to this.

$$\mathbf{k}_P = \frac{1}{\sqrt{2}} \begin{bmatrix} S_{HH} + S_{VV} \\ S_{HH} - S_{VV} \\ S_{HV} + S_{VH} \\ i(S_{HV} - S_{VH}) \end{bmatrix} \equiv \begin{bmatrix} a \\ b \\ c \\ d \end{bmatrix}. \quad (2.14)$$

The primary advantage of this basis is that it provides a direct physical interpretation of elementary scattering mechanisms. Consequently, the squared magnitude of each Pauli component quantifies the contribution of a specific canonical mechanism to the total radar cross-section (RCS). Specifically:

- Single-bounce:  $|a|^2/2$  corresponds to odd-bounce scattering, typically arising from spheres, flat plates, or trihedral reflectors. In an automotive context, this mechanism dominates returns from flat surfaces, such as walls or the rear of a vehicle.
- Double-bounce:  $|b|^2/2$  corresponds to even-bounce scattering derived from dihedral structures. This is commonly observed in the corner-like features of a car (e.g., window frames and side mirrors) or the ground-wall interaction of a curb.
- Cross-polar:  $|c|^2/2$  represents the cross-polarization energy induced by dihedrals or dipoles rotated by  $45^\circ$  around the radar line-of-sight.
- Asymmetric:  $|d|^2/2$  accounts for non-reciprocal scattering mechanisms or asymmetric geometries which convert horizontal to vertical polarization differently than vice versa.

In strict monostatic configurations, the principle of reciprocity applies, theoretically forcing the fourth component to zero; practically, it will contain noise or system artefacts. In the ideal scenario of  $d = 0$ , the Pauli vector reduces to a three-dimensional representation:

$$\mathbf{k}_P \equiv \mathbf{k}_P = \begin{bmatrix} a \\ b \\ c \end{bmatrix} = \frac{1}{\sqrt{2}} \begin{bmatrix} S_{HH} + S_{VV} \\ S_{HH} - S_{VV} \\ 2S_{HV} \end{bmatrix}. \quad (2.15)$$

However, in the *quasi-monostatic* scenarios relevant to this work – where transmit and receive antennas are closely spaced but not co-located – the asymmetry term  $d$  may contain non-negligible system noise or phase imbalances which must be accounted for during calibration.

---

<sup>4</sup>The scaling factor of  $\sqrt{2}$  ensures that the Euclidean norm of the target vector matches the Frobenius norm of the scattering matrix, thereby satisfying the requirement for ‘total power invariance’. The same reasoning applies to the lexicographic basis discussed later.

**Lexicographic basis.** An alternative representation frequently encountered in the literature is the *lexicographic basis*, which is a scaled canonical basis of  $\mathbb{C}^{2 \times 2}$ :

$$\Phi_L = \left\{ 2 \begin{bmatrix} 1 & 0 \\ 0 & 0 \end{bmatrix}, 2 \begin{bmatrix} 0 & 1 \\ 0 & 0 \end{bmatrix}, 2 \begin{bmatrix} 0 & 0 \\ 1 & 0 \end{bmatrix}, 2 \begin{bmatrix} 0 & 0 \\ 0 & 1 \end{bmatrix} \right\}. \quad (2.16)$$

This basis orders the target vector elements as  $\mathbf{k}_L = [S_{HH}, S_{HV}, S_{VH}, S_{VV}]^T$ . While is the native format for many radar hardware interfaces and is convenient for system calibration, it lacks the direct physical interpretability of the Pauli basis.

**Alternative decompositions.** While Krogager and Cameron proposed alternative coherent decompositions – such as Krogager’s approach using circular polarization to decompose targets into sphere, diplane, and helix components<sup>5</sup> – the Pauli basis remains the standard for coherent preprocessing due to its orthogonality and computational efficiency.

### 2.2.2 Incoherent decomposition

In the context of VRU classification, targets are rarely simple point scatterers. A pedestrian, for instance, is a complex aggregate of limbs with varying orientations and materials, possibly moving within a single resolution cell, creating a *distributed target*. To analyse such targets, it is necessary to move from the coherent vector  $\mathbf{k}_P$  to the second-order statistics represented by the *Pauli coherency matrix*  $\mathbf{T}$ , defined as a statistically averaged outer product of the Pauli vector:<sup>6</sup>

$$\mathbf{T} = \langle \mathbf{k}_P \cdot \mathbf{k}_P^\dagger \rangle, \quad (2.17)$$

where  $\langle \cdot \rangle$  denotes statistical averaging over an arbitrary dimension.<sup>7</sup> This matrix is Hermitian positive semidefinite and, as such, is always diagonalizable by a unitary matrix  $\mathbf{U}$ , formed by orthonormal eigenvectors of  $\mathbf{T}$ , and the diagonalized matrix  $\mathbf{D}$  features non-negative real entries on its main diagonal, which are the eigenvalues of  $\mathbf{T}$ .

It is worth noting that  $\mathbf{T}$  is, under unitary transformation, mathematically equivalent to any matrix formed by an outer product of the Sinclair scattering matrix, regardless of the decomposition basis used for vector representation. This means that the lexicographic basis introduced in Equation (2.16), as well as the Krogager circular and Cameron bases discussed above, can all be employed, making the following analysis techniques broadly applicable.

The most established method for analysing the coherency matrix, originally developed by Cloude and Pottier in 1997 for SAR imaging and remote sensing, is the *Cloude-Pottier decomposition*, which assumes that there is always a dominant average scattering mechanism in each cell. To generate estimates of the average target scattering matrix parameters, this method employs the eigenvalue expansion; that is

$$\mathbf{T} = \sum_{i=1}^3 \lambda_i \mathbf{e}_i \mathbf{e}_i^\dagger, \quad (2.18)$$

where are the eigenvalues, sorted in descending order ( $\lambda_1 \geq \lambda_2 \geq \lambda_3$ ), and  $\mathbf{e}_i$  are the orthogonal eigenvectors.

---

<sup>5</sup>This is analogous to the Pauli decomposition but employs a circular polarization basis, which can be advantageous for identifying certain target geometries. While the components share similar interpretations (single-bounce and double-bounce), the helix component is physically distinct from Pauli’s ‘tilted-wall component’; it captures chiral or asymmetric scattering mechanisms that are not explicitly represented as a unique shape in the Pauli basis.

<sup>6</sup>The Pauli coherency matrix  $\mathbf{T}$  should not be confused with the general coherency matrix  $\mathbf{J}$  defined in Equation (2.7), which is a  $2 \times 2$  matrix representing the wave’s polarization state. While both are coherency matrices, they serve different purposes:  $\mathbf{J}$  characterizes the polarization of the electromagnetic wave itself, whereas  $\mathbf{T}$  encapsulates the statistical scattering properties of the target as represented in the Pauli basis.

<sup>7</sup>In SAR polarimetry, this averaging is typically performed over multiple looks or spatial pixels to reduce speckle noise. In automotive radar, where real-time processing is essential, this averaging may be performed temporally over multiple pulses or spatially across adjacent range, Doppler, or angle-of-arrival cells.

**Noise subspace reduction** In a practical measurement utilizing the full 4D Pauli vector (Eq. 2.14), the coherency matrix is  $4 \times 4$  with four eigenvalues. However, under the monostatic assumption, the physical signal subspace is rank-3. As discussed by Visentin [5], the fourth eigenvalue  $\lambda_4$  can be attributed to additive white Gaussian noise (AWGN) in the non-reciprocal channel. To enhance estimation accuracy, a noise subtraction step is often applied:

$$\lambda'_i = \lambda_i - \lambda_4 \quad \text{for } i = 1, 2, 3, \quad (2.19)$$

assuming  $\lambda_4$  represents the noise floor  $N$ . Following this correction, the analysis proceeds on the reduced  $3 \times 3$  subspace.

The resulting unitary matrix  $\mathbf{U} = [\mathbf{e}_1 \ \mathbf{e}_2 \ \mathbf{e}_3]$  contains eigenvectors parametrized by five angular degrees of freedom, specifically:

$$\mathbf{e}_i = \begin{bmatrix} \cos(\alpha_i)e^{i\epsilon_i} \\ \sin(\alpha_i)\cos(\beta_i)\exp(i\delta_i) \\ \sin(\alpha_i)\sin(\beta_i)\exp(i\gamma_i) \end{bmatrix}, \quad i = 1, 2, 3. \quad (2.20)$$

Based on this eigendecomposition, three key parameters are defined. First, defined from the logarithmic probability of the eigenvalues, the *polarimetric entropy* measures the ‘randomness’ of the scattering process:

$$H = -\sum_{i=1}^3 P_i \log_3(P_i), \quad \text{where} \quad P_i = \frac{\lambda'_i}{\sum_{k=1}^3 \lambda'_k}. \quad (2.21)$$

This definition delineates the scattering processes:  $H = 0$  indicates a fully deterministic, single dominant mechanism without loss of polarimetric information, such as an isotropic point target, while  $H = 1$  indicates random noise or fully developed volumetric scattering with complete depolarization effects, such as dense foliage or complex clutter.

Second, the angle  $\alpha_i$  is defined using the angular parametrization of eigenvectors from Equation (2.20) to identify the physical mechanism associated with the  $i$ -th eigenvalue. This polarimetric classifier, known as the *mean alpha angle*, is defined as

$$\bar{\alpha} = \sum_{i=1}^3 P_i \alpha_i. \quad (2.22)$$

This feature effectively categorizes scattering mechanisms into three primary types:

- $\bar{\alpha} \approx 0^\circ$ : isotropic surface (road, car body).
- $\bar{\alpha} \approx 45^\circ$ : dipole/volume (vegetation, potentially limbs).
- $\bar{\alpha} \approx 90^\circ$ : isotropic dihedral (ground-wheel, curb).

It should be noted that  $\alpha$  strongly depends on the angle of incidence; flat surfaces tend to yield lower  $\alpha$  values at normal incidence and higher values at grazing angles due to varying reflection coefficients.

Finally, the *polarimetric anisotropy* is another parameter defined as an eigenvalue ratio, constructed as a complementary description to entropy. It characterizes the relative importance of the second and third eigenvalues with respect to their descending arrangement:

$$A = \frac{\lambda_2 - \lambda_3}{\lambda_2 + \lambda_3}. \quad (2.23)$$

This metric ranges from  $A = 0$ , indicating equal contributions from the second and third scattering mechanisms, to  $A = 1$ , where the third mechanism is negligible relative to the second.

Polarimetric anisotropy thus describes the complexity of the non-dominant scattering, providing a means to differentiate between targets that may exhibit similar entropy values.

Anisotropy is particularly meaningful when the entropy is high ( $H > 0.7$ ): in this regime, it distinguishes between targets with two significant scattering mechanisms (high  $A$ ) and those characterized by fully random or isotropic scattering (low  $A$ ). When entropy is low, the second and third eigenvalues are typically too small for anisotropy to provide reliable information, limiting its interpretability in such cases.

**The  $H/\alpha$  plane.** The joint analysis of polarimetric entropy  $H$  and mean alpha angle  $\bar{\alpha}$  provides a powerful two-dimensional feature space for target classification, commonly referred to as the  $H/\alpha$  plane. This representation allows for intuitive visualization and separation of different scattering mechanisms, especially in SAR polarimetry, based on their polarimetric characteristics.

### 2.2.3 Simple polarimetric descriptors

While the target decomposition theorems discussed in Section 2.2.1 and Section 2.2.2 offer rigorous physical interpretations of the scattering mechanisms, their computational complexity – requiring eigendecomposition of the  $3 \times 3$  coherency matrix for every resolution cell – can be prohibitive for real-time automotive applications constrained by embedded hardware resources. Consequently, simple polarimetric descriptors – originally developed for hydrometeor classification [8] based on power ratios and correlation coefficients – can offer low-complexity proxies for target classification. However, the translation of these metrics from meteorological bands (S/C/X-band) to automotive millimetre-wave frequencies (77 GHz to 81 GHz) requires careful consideration of wavelength-scale roughness and system limitations.

**Differential reflectivity.** Perhaps the most fundamental polarimetric ratio, differential reflectivity quantifies the power imbalance between horizontal and vertical polarizations. It is defined logarithmically as

$$Z_{\text{DR}} = 10 \log_{10} \left( \frac{\langle |S_{\text{HH}}|^2 \rangle}{\langle |S_{\text{VV}}|^2 \rangle} \right). \quad (2.24)$$

In meteorology, this metric serves as a feature for classifying raindrop oblateness. In the automotive context,  $Z_{\text{DR}}$  provides a measure of the target's geometric orientation. Passenger vehicles, being predominantly horizontally oriented structures, typically exhibit positive  $Z_{\text{DR}}$ . Conversely, pedestrians lack this stable horizontal dominance; their scattering response at 79 GHz is distributed and fluctuating due to the roughness of clothing and limb motion [9], often resulting in a mean  $Z_{\text{DR}}$  near 0 dB. Thus,  $Z_{\text{DR}}$  acts as a robust discriminator for separating vehicles from non-horizontal clutter.

**Linear depolarization ratio.** The linear depolarization ratio measures the system's ability to detect cross-polarized energy relative to the co-polarized return. It is defined as

$$\text{LDR} = 10 \log_{10} \left( \frac{\langle |S_{\text{VH}}|^2 \rangle}{\langle |S_{\text{VV}}|^2 \rangle} \right). \quad (2.25)$$

An ideal monostatic radar observing a sphere or a flat plate at normal incidence results in zero cross-polarization ( $\text{LDR} \rightarrow -\infty$ ). In contrast, complex targets with intricate geometries, such as bicycles, induce significant depolarization due to multiple scattering and non-orthogonal structural components [10]. This can result in elevated LDR values compared to flat plates, though detecting this weak cross-polarized return requires high SNR. Practically, however, the utility of this metric is bounded by the antenna system's cross-polarization isolation: If

Add figure of  $H/\alpha$  plane with typical target clusters.

the antenna leakage exceeds the target’s depolarization response, the LDR signature becomes corrupted, limiting its use to high-performance sensor architectures.

**Co-polar correlation coefficient.** To assess the coherence between the horizontal and vertical scattering centres, the co-polar correlation coefficient is utilized:

$$\rho_{hv} = \frac{|\langle S_{HH} S_{VV}^* \rangle|}{\sqrt{\langle |S_{HH}|^2 \rangle \langle |S_{VV}|^2 \rangle}}. \quad (2.26)$$

This statistical descriptor ranges from 0 to 1 and is potentially the most robust metric for automotive scenes. Man-made objects with stable phase centres, such as vehicles, poles, guardrails, typically exhibit  $\rho_{hv}$  close to 1. In contrast, distributed volume scatterers – such as bushes, grass, and tree canopies – decorrelate the orthogonal channels significantly due to their random orientation and depth, yielding lower correlation values. This could make  $\rho_{hv}$  an effective pre-filter for suppressing vegetation clutter, a common source of false positives in radar perception.

These descriptors can be computed efficiently for each resolution cell and used as input features to lightweight classification algorithms. For example, objects exhibiting very large negative LDR values alongside high  $\rho_{hv}$  are likely to correspond to specular reflections off the road surface and buildings, which can be filtered out early.

#### 2.2.4 Gap analysis: Doppler-resolved polarimetric signatures

The decomposition methods discussed in Sections 2.2.1 and 2.2.2 generally treat the radar target as a singular spatial entity. However, for dynamic VRU classification, a purely spatial perspective is insufficient. Pedestrians and cyclists are articulate structures characterized by complex motion, generating a unique spectral signature known as the *micro-Doppler* effect.

While micro-Doppler analysis is conventionally performed on scalar spectrograms, the physical scattering mechanisms of limbs and wheels are non-stationary. Therefore, the polarimetric features should theoretically vary as a distributed function over the Doppler domain.

**Validation of the polarimetric-Doppler hypothesis.** Recent experimental work has validated the conjecture that resolving polarimetry in the Doppler domain yields distinct, semantic classification features. As demonstrated by Bouwmeester et al. [10], the scattering mechanisms of VRUs are not constant but evolve across the gait cycle. Using a standard  $3 \times 4$  MIMO configuration (12 virtual channels) in a diagonal polarization basis, the study confirmed that specific micro-Doppler components exhibit unique polarimetric behaviours:

- *Cyclists:* While the frame and rider exhibit dominant odd-bounce scattering (high Pauli  $a$  and  $b$  features), the rear wheel introduces a distinct cross-polarized response (Pauli  $c$  feature) corresponding to a dihedral mechanism, likely due to the spoke-rim interaction.
- *Pedestrians:* The torso and forward-swinging limbs exhibit predominantly co-polarized returns, whereas backward-swinging limbs show weak depolarization.

By feeding these Doppler-resolved polarimetric power maps into a convolutional neural network, an F1-score of 98.2% was achieved, statistically outperforming single-polarization baselines and confirming the utility of the feature set.

**The spatial resolution bottleneck.** Despite validating the phenomenological benefits of polarimetric micro-Doppler, the current state of the art faces a critical limitation regarding spatial separability. To manage the computational load and the limited angular resolution of a standard 12-channel virtual array, the processing pipeline proposed by Bouwmeester et al. [10] relies on a ‘dominant target’ selection strategy:

‘The angle for which the sum of the squared absolute values of the scattering matrix is maximum is computed...This procedure effectively selects the dominant target within a range-Doppler cell, thus removing the angular dimension from the processed measurement data.’

While effective in controlled, isolated scenarios, this approach creates a significant reliability gap in complex urban environments. In a realistic traffic scene, a VRU is frequently spatially adjacent to strong static reflectors (e.g., fences, guardrails, or parked vehicles). If a pedestrian and a static object co-exist within the same range-Doppler bin, the polarimetric signature of the dominant clutter will mask the subtler polarimetric features of the VRU limbs. Consequently, low-resolution estimates of entropy  $H$  and anisotropy  $A$  become contaminated, rendering the classification features ambiguous.

**Research objective.** To advance beyond this dominant-target limitation, the radar architecture must possess sufficient angular resolution to spatially isolate dynamic VRUs from clutter *before* polarimetric feature extraction. This necessitates a transition from standard low-order MIMO to large-aperture MIMO topologies.

This project proposes a scaled  $12 \times 16$  MIMO architecture yielding up to 192 virtual channels. By leveraging this large virtual aperture, the system aims to preserve the angular dimension, allowing for the extraction of clean, spatially isolated scattering matrices for every Doppler bin. Consequently, the primary research question of this work is defined as:

Can the integration of a high-resolution  $12 \times 16$  MIMO architecture with Doppler-resolved polarimetric processing significantly enhance the classification accuracy of dynamic VRUs?

# Chapter 3

## Front-end technologies

The antenna element serves as the fundamental physical interface of the radar sensor, defining the initial boundary conditions for signal fidelity. In the context of polarimetric MIMO automotive radar operating in the 77 GHz to 81 GHz band, the antenna design is governed by a stringent conflict between electromagnetic purity and mass-producibility. While the synthesis of large virtual apertures relies on the placement of these elements, the quality of the polarimetric information is determined by the individual element's ability to maintain orthogonal polarization states over a wide field of view (FOV).

Achieving high cross-polarization discrimination (XPD) at millimetre-wave frequencies is notoriously difficult, particularly when constrained by the low-profile, cost-sensitive packaging requirements of the automotive industry. The antenna must not only exhibit robust isolation and gain stability but also mitigate the effects of surface waves and mutual coupling, which can degrade the orthogonality of the MIMO channels. Consequently, the choice of antenna technology is not merely a component selection but a system-level architectural decision that dictates the achievable dynamic range of the polarimetric radar.

### 3.1 Design requirements and constraints

The transition from standard automotive radar to fully polarimetric imaging imposes a specific set of performance metrics that narrow the field of viable antenna topologies. The primary driver is polarization purity across the scan volume: whereas legacy systems prioritize gain, a polarimetric sensor requires an XPD exceeding 20 dB across a wide azimuth FOV (typically up to  $\pm 60^\circ$ ) [4]. This is challenging because the geometric projection of polarization vectors' orthogonality naturally degrades at oblique angles [11].

Furthermore, these electromagnetic requirements must be reconciled with the realities of automotive integration. The antenna must be compatible with standard multi-layer printed circuit board (PCB) or package-level – typically ball grid array (BGA) or embedded wafer level BGA (eWLB) – manufacturing processes, usually precluding bulky metallic waveguide flanges or machined horns. Furthermore, mutual coupling becomes a critical parameter in dense MIMO arrays; insufficient isolation between co-located orthogonal ports of dual-polarized antenna elements can lead to signal leakage that is mathematically indistinguishable from target depolarization. Finally, thermal stability is non-negotiable; the phase centre and resonant frequency must remain stable under the harsh temperature cycling of an automotive environment to prevent calibration drift in the virtual array manifold [12].

### 3.2 Overview of radar front-end technology

The literature presents a diverse array of structural architectures proposed for 79 GHz operation. These can be broadly categorized into planar printed structures – which dominate

the current commercial landscape – and substrate-integrated or waveguide-based solutions that offer performance enhancements at the cost of manufacturing complexity.

### 3.2.1 Planar printed technology

The *microstrip patch antenna* remains the standard radiating element for commercial automotive radar due to its seamless integration with low-cost multi-layer PCB processes [1]. In polarimetric applications, dual-polarized operation is typically achieved using orthogonal feeds (aperture-coupled or probe-fed) or proximity-coupled patches [13, 14, 15]. While highly manufacturable, patch antennas suffer from intrinsic limitations at microwave frequencies: they are prone to high dielectric loss and surface wave excitation which degrade efficiency and coupling, and their narrow impedance bandwidth can be a bottleneck for wideband chirps [16]. Moreover, maintaining high XPD at wide angles is difficult due to the inevitable cross-polar radiation from the feed lines. Microstrip stub antennas, which utilize shaped stubs for improved impedance bandwidth and polarization control, pose a compelling alternative to conventional series patch arrays for compact, low-profile implementations [17].

Antenna elements based on *slotted radiation*, including cavity-backed slots and slanted slot arrays, offer an alternative planar approach. Slots naturally exhibit high polarization purity and can be more robust against mutual coupling than patches [18, 19]. However, they are intrinsically single-polarized, and hence, integrating dual-polarized slot arrays often requires multi-layer feed networks [20] that increase board complexity, and their bidirectional radiation pattern usually necessitates a back-cavity or reflector, adding to the vertical profile.

Emerging in the recent years, *thin-film antennas* leverage advanced deposition techniques to realize ultra-thin radiating structures directly on the substrate [21]. While thin-film designs can support dual-polarization and flexible integration, they are typically very lossy at millimetre-wave frequencies, which limits their efficiency and practical deployment in automotive radar systems.

### 3.2.2 Integrated waveguide technology

To overcome the loss mechanisms of microstrip lines, *substrate integrated waveguide* (SIW) and *low temperature co-fired ceramic* (LTCC) technologies confine the electromagnetic field within a synthesized waveguide structure embedded in the dielectric. SIW antennas exhibit significantly lower transmission losses and superior element isolation compared to microstrip [22]. Their enclosed nature provides excellent shielding, making them robust against interference and temperature-induced deformations. However, the requisite via-fencing consumes considerable board real estate, posing a challenge implementing dense MIMO lattices without sacrificing grating lobe performance.

*Gap waveguide* (GW) and *ridge gap waveguide* (RGW) technologies represent a significant evolution in low-loss millimetre-wave design, addressing the assembly bottlenecks of traditional hollow waveguides. By utilizing an electromagnetic band-gap (EBG) surface, such as the ‘bed of nails’ reported by Kildal et al. [23], to suppress parallel-plate modes, GW technology achieves the low loss of air-filled waveguides while eliminating the requirement for conductive electrical contact between waveguide layers.

This ‘contactless’ characteristic creates a unique advantage for automotive radar: it relaxes the stringent mechanical flatness and assembly torque requirements that drive up the cost of traditional split-block waveguides. While early iterations relied on costly CNC milling, recent advancements in metallized plastic injection moulding and PCB-based implementations (using via fences or mushroom structures) have drastically reduced fabrication costs, as validated in the industrial study by [24]. Consequently, GWs are transitioning from academic demonstrators to commercial viability, offering a robust solution for high-efficiency, fully metallic antenna arrays capable of withstanding the harsh thermal and vibrational environments of automotive sensing [25].

This ‘contactless’ characteristic creates a unique advantage for automotive radar: it relaxes the stringent mechanical flatness and assembly torque requirements that drive up the cost of traditional split-block waveguides. While early iterations relied on costly CNC milling, recent advancements have enabled a transition to metallized plastic injection moulding. As detailed in industrial studies by Bencivenni et al. [24] and Huegel et al. [26], this approach allows for the rapid prototyping of complex layers via 3D printing before scaling to high-precision injection moulding for mass production. This workflow effectively shifts the complexity from assembly to the mould-design phase, resulting in high-efficiency, air-filled waveguide arrays commercially viable for the harsh thermal and vibrational environments of automotive sensing [25].

### 3.2.3 Volumetric antennas

While impractical for conformal automotive integration, *horn antennas* and *dielectric resonator antennas* (DRAs) serve as important benchmarks, hence their use in polarimetric system demonstrators, such as those presented by Tinti et al. [4] and Trummer et al. [27]. Horns exhibit outstanding gain and polarization discrimination but are volumetrically incompatible with bumper-integrated sensors. DRAs offer wide bandwidth and high radiation efficiency by eliminating metallic losses [28], yet they face challenges regarding mechanical robustness and the precision assembly required to mount 3D dielectric blocks onto a planar radar transceiver.

**Launcher-in-package technology.** In recent years, launcher-in-package (LiP) technology has emerged as a promising solution to the traditional challenges of integrating waveguide antennas with monolithic microwave integrated circuits (MMICs). By embedding the waveguide transition directly within the package substrate, LiP minimizes the number of RF transitions, thereby reducing insertion loss and reflection typically associated with conventional chip-to-waveguide interfaces [29]. While still an emerging technology, this advancement enables more efficient coupling between the transceiver and the antenna, making waveguide-based solutions more viable for compact automotive radar systems.

## 3.3 Comparative analysis of antenna technologies

A critical review of the literature reveals that antenna performance is not determined by a single design choice, but rather by the interaction between two distinct layers: the *radiating element* and the *integration platform*. In many reported designs, these two aspects are conflated. To provide a clearer map of the design space, this analysis decouples these layers, evaluating them separately before synthesizing the state-of-the-art findings.

### 3.3.1 Radiating element typologies

The choice of radiating element dictates the intrinsic bandwidth, polarization discrimination, and radiation pattern of the sensor. Table 3.1 categorizes the fundamental element types found in automotive radar literature.

While microstrip patches dominate commercial implementations due to their low profile, they are intrinsically narrowband and prone to surface wave excitation. In contrast, volumetric radiators like horns and DRAs offer superior bandwidth and polarization stability but face severe integration penalties. Slot radiators occupy a middle ground, offering high XPD but requiring complex back-cavity structures to suppress bidirectional radiation.

### 3.3.2 Integration platforms

The integration platform defines the feeding structure of the antenna system: it determines insertion loss, isolation between MIMO channels, and thermal stability. As shown in Table 3.2,

the industry standard (microstrip/PCB) trades performance for cost, while academic research heavily favours waveguide-based structures to maximize signal fidelity.

Table 3.1: Comparison of radiating element types for polarimetric radar

Element type	BW (%)	XPD (dB)	Profile	References
Edge-fed patch	< 5	15–20	Very low	[30, 31, 32]
Aperture-coupled patch	5–15	20–30	Low	[14, 22, 33, 34, 35]
Microstrip stub	< 5	20–25	Very low	[17, 36]
Thin-film antenna	~ 10	20–30	Very low	[21]
Slotted waveguide	< 5	15–25	Low	[37, 38]
Cavity-backed slot	< 5	> 25	Moderate	[18, 19, 20, 39, 40]
Horn waveguide	> 15	> 25	High (3D)	[4, 27, 41]
Dielectric resonator	10–15	~ 20	High (3D)	[28, 42]

Table 3.2: Comparison of integration and feeding platforms

Platform	Loss	Isolation	Complexity	References
Planar PCB	High	Low	Very low	[17, 30, 31, 32, 36]
Multi-layer PCB	Moderate	Moderate	Moderate	[22, 39, 43]
Metallic waveguide	Very low	Very high	Moderate	[4, 18, 27, 44]
SIW	Moderate	High	Moderate	[19, 33, 35, 37, 40, 41]
LTCC	Low	High	High	[38]
Gap waveguide	Low	Very high	High	[16, 45]

### 3.4 Synthesis of state-of-the-art trends

Analysing the intersection of these element and platform choices reveals a clear dichotomy in the current state of the art.

**Industrial baseline.** Despite their electromagnetic limitations, microstrip patch arrays remain the incumbent solution for mass-market automotive radar. The manufacturing maturity of standard PCB processes allows for the low-cost integration of complex series-fed or series-parallel networks directly alongside the MMIC [46]. However, for polarimetric applications, this convenience comes at a cost: standard patches struggle to maintain XPD beyond  $\pm 30^\circ$  scan angles [40], and the mutual coupling between closely spaced elements in a dense MIMO array introduces phase errors that degrade virtual aperture synthesis and the performance of signal processing algorithms, as explored by Arnold and Jensen [47].

**Performance frontier.** Recent academic literature identifies GW and RGW as the primary candidates for overcoming the inherent dielectric losses and surface-wave coupling of high-frequency PCB technology. By creating a prohibiting EBG, GW structures suppress parallel-plate modes entirely without requiring a galvanic connection between the waveguide layers. This ‘contactless’ property is a critical industrial enabler; it significantly relaxes the mechanical assembly tolerances that make traditional hollow waveguides cost-prohibitive for high-volume

production. Through the adoption of metallized injection moulding and high-precision plastic stamping, the manufacturing complexity is shifted from individual assembly to the mould-design phase, allowing for the low-cost mass production of air-filled structures. Consequently, GW technology, particularly in combination with the LiP technology, represents the emerging ‘gold standard’ for next-generation MIMO arrays, providing the polarimetric fidelity and thermal robustness required for high-resolution automotive sensing within a commercially viable form factor [48].

**The compromise.** SIW architectures effectively bridge the gap between planar and volumetric designs. By synthesizing a dielectric-filled waveguide using periodic via fences, SIW provides the electromagnetic shielding and low-loss characteristics of metallic waveguides while retaining the manufacturability of standard PCBs. The versatility of this platform is exemplified by Zhao et al. [41], who demonstrated that multi-layer PCB stacks can be used to synthesize quasi-pyramidal horn antennas entirely within the substrate.

Furthermore, the layered structure of SIW facilitates advanced hybrid topologies. For instance, designs by Puskely et al. [33] and Yang et al. [40] combine the isolation benefits of an integrated waveguide feed with the beam-shaping flexibility of printed elements, using coupling slots in a sandwiched ground layer to excite parasitic patches on the surface.

In parallel, LTCC technology offers a similar volumetric approach but with superior thermal stability and dimensional tolerance compared to organic substrates, making it attractive for highly integrated package-level antennas, albeit at a higher implementation cost.

### 3.5 Emerging paradigms

Beyond the established categories of printed and waveguide-based elements, several exploratory technologies are expanding the design space for automotive radar. These paradigms prioritize the synthesis of ideal radiation characteristics over traditional fabrication constraints.

**Magneto-electric dipoles (MED).** Originally developed to overcome the narrow bandwidth of standard patch antennas, the magneto-electric dipole has recently been adapted for millimetre-wave radar to address the specific requirements of polarimetric fidelity. By combining a planar electric dipole with a complementary magnetic dipole (typically synthesized via shorted patches or via-fenced slots), MEDs function effectively as Huygens sources.

This complementary excitation yields two distinct advantages for automotive sensing. First, it achieves wide impedance bandwidths (usually  $> 20\%$ ), easily covering the full 76 GHz to 81 GHz band required for high-resolution 4D imaging [49]. Second, and more critically for polarimetry, MEDs exhibit nearly identical E- and H-plane radiation patterns with low cross-polarization. This pattern symmetry ensures that the radar’s ‘view’ of a target is consistent regardless of polarization orientation, potentially simplifying the calibration matrices required for precise direction-of-arrival (DOA) estimation.

**Metasurface-enhanced isolation.** As MIMO arrays become denser to support higher angular resolution, mutual coupling via surface waves becomes a dominant source of error. Designers are increasingly leveraging metasurfaces – periodic sub-wavelength structures etched into the PCB ground or top layer – to manipulate these boundary conditions.

Rather than functioning as radiating elements themselves, these structures often act as EBG filters or soft surfaces. By presenting a high surface impedance to grazing waves, they effectively trap or dissipate surface currents between adjacent patch elements. Recent implementations have demonstrated isolation improvements of 10 dB to 20 dB with negligible impact on the primary radiation pattern, offering a planar solution to the coupling problems that traditionally required metallic wall isolation [50].

**Additive manufacturing and integrated lenses.** Recent advances in high-precision additive manufacturing are transforming the landscape of millimetre-wave antenna prototyping. Unlike traditional machining or moulding, 3D printing enables the fabrication of complex waveguide structures with intricate internal geometries, such as non-standard transitions, that are otherwise impossible to manufacture. While currently more suited to rapid prototyping than high-volume automotive deployment, this technology offers a unique pathway for validating complex volumetric designs before committing to expensive tooling.

A compelling application of this paradigm is the direct 3D printing of integrated lens antennas, where dielectric lenses, such as Luneburg or Maxwell fish-eye profiles, are fabricated as part of the antenna structure [51]. This approach enables volumetric gain enhancement within a compact footprint, but remains limited by the loss tangent and surface roughness of available printable materials, which can introduce additional losses and phase errors at 79 GHz. While promising for prototyping and specialized applications, further advances in printable materials and post-processing are needed for widespread automotive deployment.

### 3.6 Design implications

The survey of the literature leads to a specific set of design directions for the polarimetric MIMO demonstrator targeted in this work. While GW technology offers the highest theoretical performance, its fabrication complexity poses a risk for rapid prototyping. Conversely, microstrip patches offer a low-risk, low-cost baseline but are likely to bottleneck the polarimetric dynamic range of the system.

Therefore, a pragmatic high-performance approach points toward SIW-based topologies or advanced cavity-backed slot designs. These architectures offer the requisite isolation and polarization stability to validate sparse polarimetric MIMO algorithms, while remaining within the bounds of standard PCB fabrication capabilities.

The preceding review captures a vast and rapidly evolving design space for 79 GHz automotive radar. It is evident that emerging technologies, particularly GW as an integration platform and MEDs as radiating elements, are maturing into robust solutions that address the traditional losses and bandwidth limitations of millimetre-wave circuitry. These technologies represent the state of the art of electromagnetic design, offering superior isolation and polarization purity that are highly attractive for next-generation sensing.

However, the architectural choices for the specific research encompassed by this project are governed by a different set of optimization criteria. The primary objective of this doctoral work is the extraction of dynamic, Doppler-resolved polarimetric signatures using a large-aperture MIMO radar. In this context, the antenna array is not the primary subject of innovation but rather an enabler – a critical functional block that must guarantee reliable data acquisition to validate the signal processing techniques of polarimetric decomposition and signature extraction.

Consequently, the focus is placed on the ability to rapidly prototype a complete, reliable polarimetric system with imaging capabilities, rather than employing experimental radiating elements that may introduce manufacturing uncertainties or integration delays. To align with this objective, the following design decisions have been established:

- **Adoption of planar technology:** To attain industrial support in terms of manufacturability and compatibility with standard calibration routines, the design is restricted to planar technologies (PCB/LTCC). While acknowledging the superior efficiency of air-filled waveguides, the mature fabrication processes of printed circuits ensure that the large-scale MIMO array can be produced with consistent tolerances, which is a prerequisite for accurate array manifold calibration.
- **Selection of radiating mechanism:** Within the planar domain, the design strategy envisions a multi-layer SIW stack-up as the high-performance contender. Specifically,

slotted radiation serves as the main mechanism, potentially augmented with parasitic patches on the top layer to shape the individual beam pattern and improve impedance bandwidth, a technique supported by recent studies on hybrid SIW-patch topologies, such as works of Puskely et al. [33] and Yang et al. [40]. This approach strikes a balance between the isolation benefits of substrate-integrated waveguides and the low profile of printed elements.

- **Iterative development strategy:** To mitigate risk, particularly in the early phases of the project, the front-end design will leverage the established experience of dealing with uniform patch array cascades. This approach mirrors the proven architectures employed by industry leaders, such as Texas Instruments [52] and Continental, for imaging automotive radar. By starting with a known baseline – standard series-fed microstrip patches – the research ensures a stable platform for initial data collection and algorithm development, allowing the focus to remain on the signal processing challenges of high-fidelity polarimetric measurements resolved in Doppler.

In summary, while the literature points toward GW and MED as the future of automotive electromagnetics, this research purposefully selects established planar implementations to prioritize system-level reliability and the integrity of the polarimetric signal processing pipeline.

# Chapter 4

## MIMO array design

Existing MIMO array designs for automotive radar predominantly use linear or planar layouts optimized for angular resolution and cost-efficient implementation [53]. TDM-MIMO architectures dominate current commercial systems, typically leveraging 3–4 transmitters with 4–8 receivers to synthesize virtual arrays of 12–32 channels, possibly cascading multiple such modules [52]. Recent research explores sparse 2D MIMO arrays, co-prime and nested sparse layouts, and wide-aperture imaging arrays. However, most published designs assume a single polarization, leaving the interaction between sparsity and polarization purity largely unexplored. Only a few prototypes integrate dual-polarization at W-band, and these often suffer from phase-centre mismatches, reduced aperture efficiency and severe cross-polar coupling. As a result, no established array topology exists that simultaneously optimizes spatial resolution, polarization isolation and multiplexing feasibility for a fully polarimetric automotive radar.

### 4.1 MIMO fundamentals

The concept of MIMO antenna systems is a well-established and extensively published area within telecommunications, where transmitting data over multiple uncorrelated signals results in additional information about the state of the communication channel, aggregating effects like multipath propagation and other types of signal fading or delays. This information is leveraged to estimate the channel matrix which is then used to compensate for propagation effects to recover the transmitted data.

While the foundational idea of MIMO systems has been successfully carried over to radar technology, the problem formulation is adapted: in telecommunications jargon, the primary goal of radar is to precisely estimate the channel matrix, which encapsulates the desired information about propagation effects, such as time delay, Doppler shift, and angle of arrival, allowing for extraction of target range, velocity, azimuth, and angular position [54, 55]. The success of this communications-to-radar transformation has inspired extensive research, leading to key advancements and further classifications, such as the division of the general array concept into *co-located* and *distributed* MIMO, as extensively discussed in [56, 57].

Lastly, it should be noted that the transfer of MIMO concepts from communications to radar must be undertaken with care, respecting and integrating the existing knowledge of traditional radar technology. Uncritical adaptation can lead to flawed conclusions, as seen in some early distributed MIMO literature, where certain contributions were either redundant rediscoveries of multistatic radar concepts or contained incorrect statements, as notes by Chernyak [58].

From the standpoint of antenna array design, the key feature of MIMO radar is the creation of a *virtual array* through the combination of multiple transmit and receive antennas. Mathematically, if an array has  $N_{\text{TX}}$  transmitters and  $N_{\text{RX}}$  receivers, and each transmitter emits an orthogonal waveform, the received signals can be separated and associated with each transmit-receive pair. This effectively synthesizes  $N_{\text{TX}} \times N_{\text{RX}}$  virtual elements, whose positions are determined by

the sum (or, in some cases, the difference) of the physical locations of the transmit and receive antennas [59]. The resulting virtual array, which can be obtained as a convolution of the physical transmit and receive element positions, can have a larger aperture and finer angular resolution than the physical arrays alone, but the spatial distribution of these virtual elements depends on both the physical layout and the multiplexing scheme.

**Co-located and distributed MIMO radar.** A crucial distinction exists between these two configurations. co-located MIMO radar systems feature transmit and receive antennas placed in proximity, enabling coherent transmission and detection. This coherence allows for the formation of a virtual array with enhanced angular resolution and supports advanced adaptive processing techniques. In contrast, distributed MIMO radar systems employ widely separated antennas, a technique known from multi-static radar, emphasizing on spatial diversity gain. This diversity is particularly beneficial for overcoming target scintillation (i.e. fluctuations in radar cross-section) and for improving detection performance in complex environments.

Notably, research was carried out to also explore hybrid approaches that combine the benefits of both co-located and distributed MIMO. For example, Xu and Li [60] discuss systems that leverage both coherent processing and spatial diversity, highlighting the following advantages:

- *Spatial diversity:* Widely-separated antennas in distributed MIMO configurations help mitigate target scintillation and improve detection reliability.
- *Flexible transmit beampattern design:* co-located MIMO enables optimization of the transmit covariance matrix, allowing power to be focused in directions of interest while minimizing correlation of backscattered signals. This leads to significant improvements in adaptive processing techniques.
- *Enhanced resolution and clutter rejection:* The MIMO radar scheme can achieve higher spatial resolution and improved clutter suppression compared to conventional radar systems.

The concept of combining several widely separated subarrays with each subarray containing closely spaced antennas is nowadays often implemented via *multi-aperture multiplexing* and has been successfully applied in *cooperative automotive radars*, improving angular resolution and field of view [61].

**Array architectures.** A central theme in MIMO radar design is the trade-off between spatial diversity, coherent processing gain, and hardware complexity, which is reflected in the three principal array architectures: fully diverse MIMO, phased arrays, and hybrid MIMO topologies.

In a fully diverse MIMO configuration, each antenna element operates independently, transmitting and receiving orthogonal waveforms. This maximizes spatial diversity and enables robust target detection in complex environments. Mathematically, the transmit covariance matrix in this case is full-rank, reflecting the linear independence of the transmitted signals. However, this requires a separate RF processing chain for each element, increasing hardware cost and complexity.

Phased arrays, in contrast, employ coherent waveforms across all elements, with a common signal distributed via a beamforming network. This approach enables electronic beam steering and coherent processing gain, but sacrifices spatial diversity since all elements transmit the same signal. The transmit covariance matrix is fully degenerate (rank 1), as all signals are linearly dependent.

Many modern systems adopt a hybrid approach, first introduced and called ‘phased-MIMO radar’ by Hassanien and Vorobyov [62], which combines aspects of both fully diverse MIMO and phased arrays. In these systems, groups of antenna elements form subarrays that transmit coherent waveforms, while different subarrays operate independently with orthogonal signals. The resulting transmit covariance matrix has rank between 1 and full, depending on the degree of the

so-called *waveform diversity*. This design balances the benefits of spatial diversity and coherent processing, while managing hardware complexity. The optimization of subarray partitioning and waveform assignment typically leads to a difficult, non-convex optimization problem, as discussed in the research area of *beampattern synthesis*.

## 4.2 MIMO topologies

The concept of *MIMO topology* can be defined as a mapping from the physical arrangement of transmit and receive antennas, together with the chosen multiplexing scheme, such as time-, frequency-, and code-division, onto the resulting virtual array. This mapping determines the positions and spacings of the virtual elements, which can be uniform or non-uniform depending on the physical geometry and the multiplexing strategy. Non-uniform virtual element spacing can lead to grating lobes, ambiguities, or degraded performance, making the design of the physical and virtual topology a critical aspect of MIMO radar engineering.

**Definitions & figures of merit.** The MIMO design problem can be formalized as follows: given a desired virtual array configuration (e.g. uniform linear array with specific aperture and element spacing), determine the physical transmit and receive antenna placements and the multiplexing scheme that will synthesize this virtual array. Key figures of merit for evaluating MIMO topologies include:

- *Virtual aperture*: Set of unique transmitter-receiver channels in the resulting virtual array. The aperture is often evaluated as the overall size of the virtual array, corresponding directly to the resulting *angular resolution*.
- *Field of view (FOV)*: The angular region over which the array can reliably detect and resolve targets, determined by the physical and virtual array geometry and element spacing.
- *Degrees of freedom*: The number of independent channels available for signal processing, which influences the ability to perform tasks like *direction-of-arrival estimation* and *parameter identifiability*.
- *Element spacing*: The spacing between virtual elements, affecting *grating lobes* and *ambiguity*, especially in sparse layout, where the Shannon-Nyquist spatial sampling criterion is deliberately violated.
- *Side-lobe level (SLL)*: The level of side-lobes in the virtual array's beampattern, impacting *clutter rejection* and *target detection*.
- *Mutual coupling*: The interaction between physical elements, which can distort the intended virtual array response, leading to *errors in angle estimation* or *degraded detection performance*.
- *Implementation complexity*: The practical feasibility of the physical layout and multiplexing scheme, considering hardware constraints.

### 4.2.1 Application requirements

The synthesis of MIMO topologies is fundamentally dictated by the sensing scenario, making application requirements the primary driver of array design. For automotive radar, the ability to resolve targets in both azimuth and elevation is essential, necessitating two-dimensional (2D) aperture extension. Modern front-looking automotive radar sensors, as described by Waldschmidt et al. [1], require a wide azimuth FOV of approximately  $\pm 30^\circ$  to  $\pm 60^\circ$  and a moderate elevation FOV of about  $\pm 15^\circ$  to  $\pm 30^\circ$ . These requirements exceed what can be achieved with simple

non-uniform elevation extensions of moderate-aperture linear arrays, necessitating employment of either a large element count or sparse array techniques.

However, synthesizing optimal 2D virtual arrays is challenging: the number of possible transmit-receive combinations increases rapidly, and the synthesis remains a non-deterministic optimization problem with no general closed-form solution for constructing a virtual array with ideal properties from a fixed set of physical elements. This combinatorial complexity – combined with practical constraints such as hardware cost, mutual coupling, and calibration – makes 2D MIMO topology synthesis a challenging and active research area [63].

In automotive radar, practical constraints such as limited sensor footprint and integration requirements restrict MIMO implementations almost exclusively to co-located array configurations. This spatial constraint is a systemic requirement imposed by the compact form factors and mounting locations typical of automotive platforms. As a result, the theoretical advantages of distributed MIMO – such as enhanced spatial diversity – are generally unattainable in this context.

The signal processing benefits of co-located MIMO for automotive radar are now well-established. These include the synthesis of large virtual arrays, improved angular resolution, and the ability to apply advanced adaptive processing techniques. The literature provides a comprehensive treatment of these advantages, with concepts such as parameter identifiability [64] and virtual aperture extension [65] serving as key metrics for system evaluation. The maturity of the field is further underscored by the availability of specialized reference texts dedicated to MIMO radar theory and practice [66].

Despite significant progress, two major challenges remain. First, the analytical synthesis of optimal 2D virtual arrays is still underdeveloped, leaving most practical designs reliant on numerical optimization or empirical patterns. Second, there is a pressing need to bridge the gap between electromagnetic phenomena—such as mutual coupling and parasitic effects—and signal processing algorithms, as these physical realities can introduce errors that degrade radar performance. Addressing these challenges is essential for advancing both the theoretical and practical capabilities of automotive MIMO radar.

#### 4.2.2 Topology synthesis methods

The synthesis of MIMO array topologies is a mature field offering a spectrum of design methodologies, spanning rigid analytical constructions and flexible numerical optimization techniques. Analytical approaches, particularly those governing uniform linear arrays and uniform planar arrays, provide closed-form solutions and valuable insight into the mapping between physical and virtual array geometries, typically derived using the concept of the *difference co-array* [67]. While these deterministic designs offer predictable phase centres and well-characterized point spread functions, they are often limited to specific configurations and may not generalize to constrained automotive scenarios.

For more intricate designs – such as non-uniform or highly sparse arrays, or when practical constraints like packaging and mutual coupling must be considered – numerical optimization becomes essential. In these cases, the synthesis problem is formulated using an objective function that encodes key figures of merit, including virtual aperture, side-lobe level, and ambiguity [68]. Optimization algorithms employed in this context range from evolutionary heuristics (such as genetic algorithms, simulated annealing, and differential evolution) to modern convex relaxation methods, iteratively exploring the design space to reveal Pareto-optimal trade-offs between angular resolution and side-lobe suppression [69]. However, the resulting ‘exotic’ geometries often lack translational invariance and introduce significant implementation challenges, particularly in terms of manifold calibration and mutual coupling compensation. These practical difficulties can obscure the validation of novel signal processing chains, as most optimization-driven designs assume idealized, minimum-scattering antennas – an assumption that does not hold in real-world applications and can lead to degraded processing algorithm performance [47].

**Topology classes for automotive radar.** When considering MIMO topologies for automotive applications, it is crucial to recognize the distinction between theoretical sparse concepts and industrially deployable classes.

The most established class is the uniform linear array and its two-dimensional extension, the uniform planar array. These arrays feature regularly spaced elements – typically at half-wavelength intervals ( $d = \lambda/2$ ) – resulting in an ambiguity-free field of view and direct compatibility with standard fast Fourier transform (FFT) algorithms. Their regularity is particularly advantageous for polarimetric research; it minimizes phase centre mismatch errors that can otherwise corrupt the delicate phase relationships between horizontal and vertical polarization channels. While the scalability of uniform arrays is limited by the proportional increase in hardware cost, they provide the most controlled environment for isolating and characterizing Doppler-resolved polarimetric signatures.

To address the aperture limitations of uniform arrays, structured sparse arrays have emerged as the current state-of-the-art in deployed automotive imaging radar (e.g. cascaded chipsets). Unlike the random or highly irregular sparse arrays found in theoretical literature, industrially supported sparse designs rely on specific, repeatable patterns to extend the virtual aperture. These designs offer a pragmatic compromise: they achieve the improved angular resolution necessary for modern sensing while maintaining enough structural regularity to be reliably calibrated in mass production.

**Selection rationale.** In summary, while the academic literature is rich with novel, optimization-driven antenna concepts, the development of robust polarimetric processing algorithms benefits from a stable hardware baseline. By utilizing established uniform topologies or industry-standard sparse reference designs, system variability is minimized. This ensures that observed anomalies in the Doppler-polarimetric domain can be attributed to target scattering physics rather than artefacts of an experimental antenna array manifold.

### 4.3 Polarimetric MIMO topology

The integration of polarimetric functionality into MIMO radar introduces a new dimension to topology synthesis: the management of the dual-polarized signal space. Unlike scalar MIMO (one polarization), where the primary goal is maximizing the virtual aperture, polarimetric designs must also ensure the fidelity of the full scattering matrix measurement. Consequently, the design space splits into two fundamental architectural choices: the use of dual-polarized elements sharing a common phase centre versus the spatial interleaving of single-polarized elements.

**Dual-polarized architectures.** The most theoretically robust approach involves the use of dual-polarized elements at each array position (see Figure 4.1a). In this configuration, orthogonal polarizations (typically horizontal and vertical) share a common phase centre. The primary advantage of this topology is the maximization of the virtual aperture for all polarization channels simultaneously, ensuring that the polarimetric scattering matrix is measured from an identical spatial perspective. This eliminates the ‘polarization squint’ effects caused by viewing a target from slightly different angles, thereby simplifying the calibration process.

However, this electromagnetic ideal comes with significant implementation penalties. Dual-polarized patch antennas or horn feeds require complex feeding networks, often necessitating orthogonal mode transducers (OMTs) or multilayer substrates that increase the physical bulk of the sensor. Furthermore, maintaining high isolation between the co-located channels is challenging; the proximity of the feeds invariably leads to increased mutual coupling and cross-polar leakage, which can corrupt the delicate polarimetric signature of the target.

**Interleaved single-polarized architectures.** To mitigate the hardware complexity and coupling issues of co-located designs, an alternative strategy is to spatially interleave single-polarized elements (see Figure 4.1b). By spatially separating the horizontal and vertical elements, this architecture inherently improves port-to-port isolation and simplifies the routing of feed lines. While this reduces the cost and complexity of the PCB stack-up, it introduces a spatial disparity between the polarization channels. If not carefully compensated for in the manifold synthesis, this phase centre mismatch can lead to angle-dependent polarization errors, particularly for near-field targets or distributed scatterers.

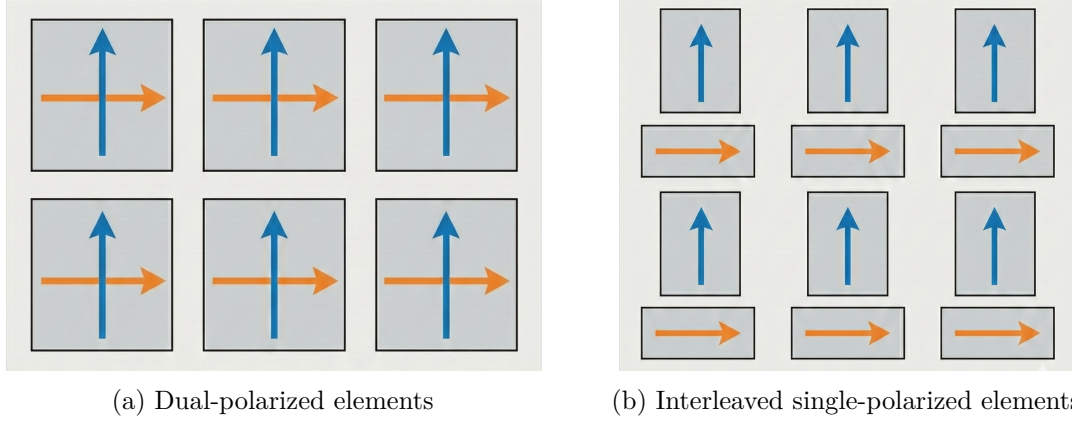


Figure 4.1: Comparison of physical element arrangements for polarimetric MIMO radar.

**Virtual channel overlapping.** A hybrid design strategy, which is worthy of investigation, is the exploitation of MIMO virtual array synthesis to bridge the gap between these two architectures. It is hypothesized that by carefully designing the overlapping patterns of transmitting and receiving sub-arrays, one can synthesize specific *virtual* positions where the co- and cross-polar channels coincide purely through signal processing, even if the physical elements are spatially separated.

This concept is illustrated in Figure 4.2. By ensuring that specific indices of the virtual convolution overlap, the system can provide ‘anchor points’ of true polarimetric alignment. These overlapping virtual phase centres could potentially serve as a high-fidelity reference for polarimetric calibration – effectively simulating the performance of a dual-polarized element – while retaining the manufacturing simplicity and isolation benefits of a single-polarized interleaved layout.

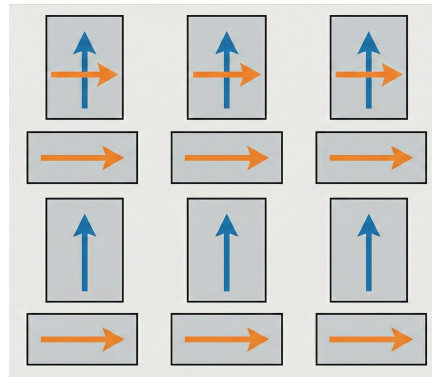


Figure 4.2: Overlapping channels in an interleaved single-polarized element grid

# Bibliography

- [1] C. Waldschmidt, J. Hasch and W. Menzel, ‘Automotive Radar — From First Efforts to Future Systems,’ *IEEE Journal of Microwaves*, vol. 1, no. 1, pp. 135–148, Jan. 2021, DOI: [10.1109/JMW.2020.3033616](https://doi.org/10.1109/JMW.2020.3033616)
- [2] J. F. Tilly, F. Weishaupt, O. Schumann, J. Dickmann and G. Wanielik, ‘Road User Classification with Polarimetric Radars,’ in *2020 17th European Radar Conference (EuRAD)*, Jan. 2021, pp. 112–115, DOI: [10.1109/EuRAD48048.2021.00039](https://doi.org/10.1109/EuRAD48048.2021.00039)
- [3] J.-S. Lee and E. Pottier, *Polarimetric Radar Imaging: From Basics to Applications*. CRC Press, 19th Dec. 2017, 474 pp.
- [4] A. Tinti, S. Tejero Alfageme, S. Duque Biarge, J. Balcells-Ventura and N. Pohl, ‘Fully Polarimetric Automotive Radar: Proof of Concept,’ *IEEE Transactions on Radar Systems*, vol. 2, pp. 645–660, 2024, DOI: [10.1109/TRS.2024.3423631](https://doi.org/10.1109/TRS.2024.3423631)
- [5] T. Visentin, *Polarimetric Radar for Automotive Applications*. KIT Scientific Publishing, 10th Apr. 2019, 188 pp.
- [6] A. Zangwill. ‘Modern Electrodynamics,’ Cambridge Aspire website, Accessed: 20th Jan. 2026. [Online]. Available: <https://www.cambridge.org/highereducation/books/modern-electrodynamics/E5448C70CBF3651B2056F28EBF859AE9>
- [7] D. Gaglione, C. Clemente, L. Pallotta, I. Proudler, A. De Maio and J. J. Soraghan, ‘Krogager decomposition and Pseudo-Zernike moments for polarimetric distributed ATR,’ in *2014 Sensor Signal Processing for Defence (SSPD)*, Sep. 2014, pp. 1–5, DOI: [10.1109/SSPD.2014.6943309](https://doi.org/10.1109/SSPD.2014.6943309)
- [8] V. N. Bringi and V. Chandrasekar, *Polarimetric Doppler Weather Radar: Principles and Applications*. Cambridge: Cambridge University Press, 2001, DOI: [10.1017/CBO9780511541094](https://doi.org/10.1017/CBO9780511541094)
- [9] Y. Deep et al., ‘Radar cross-sections of pedestrians at automotive radar frequencies using ray tracing and point scatterer modelling,’ *IET Radar, Sonar & Navigation*, vol. 14, no. 6, pp. 833–844, 2020, DOI: [10.1049/iet-rsn.2019.0471](https://doi.org/10.1049/iet-rsn.2019.0471)
- [10] W. Bouwmeester, F. Fioranelli and A. G. Yarovoy, ‘Classification of Dynamic Vulnerable Road Users Using a Polarimetric mm-Wave MIMO Radar,’ *IEEE Transactions on Radar Systems*, vol. 3, pp. 203–219, 2025, DOI: [10.1109/TRS.2025.3527884](https://doi.org/10.1109/TRS.2025.3527884)
- [11] C. Zhao, Y. Aslan and A. Yarovoy, ‘Overview of Polarimetry in Application to Automotive Radar: Array Design, Calibration and Target Feature Extraction Concepts,’ in *2025 19th European Conference on Antennas and Propagation (EuCAP)*, Mar. 2025, pp. 1–5, DOI: [10.23919/EuCAP63536.2025.10999201](https://doi.org/10.23919/EuCAP63536.2025.10999201)
- [12] M. Harter, A. Ziroff, J. Hildebrandt and T. Zwick, ‘Error analysis and self-calibration of a digital beamforming radar system,’ in *2015 IEEE MTT-S International Conference on Microwaves for Intelligent Mobility (ICMIM)*, Apr. 2015, pp. 1–4, DOI: [10.1109/ICMIM.2015.7117931](https://doi.org/10.1109/ICMIM.2015.7117931)

- [13] A. Vallecchi and G. Gentili, ‘Design of dual-polarized series-fed microstrip arrays with low losses and high polarization purity,’ *IEEE Transactions on Antennas and Propagation*, vol. 53, no. 5, pp. 1791–1798, May 2005, DOI: [10.1109/TAP.2005.846732](https://doi.org/10.1109/TAP.2005.846732)
- [14] I. Acimovic, D. A. McNamara and A. Petosa, ‘Dual-Polarized Microstrip Patch Planar Array Antennas With Improved Port-to-Port Isolation,’ *IEEE Transactions on Antennas and Propagation*, vol. 56, no. 11, pp. 3433–3439, Nov. 2008, DOI: [10.1109/TAP.2008.2005450](https://doi.org/10.1109/TAP.2008.2005450)
- [15] C. Deng, B. Yektakhah and K. Sarabandi, ‘Series-Fed Dual-Polarized Single-Layer Linear Patch Array With High Polarization Purity,’ *IEEE Antennas and Wireless Propagation Letters*, vol. 18, no. 9, pp. 1746–1750, Sep. 2019, DOI: [10.1109/LAWP.2019.2929226](https://doi.org/10.1109/LAWP.2019.2929226)
- [16] Z. Zang, Q. Ren, A. Uz Zaman and J. Yang, ‘77 GHz Fully Polarimetric Antenna System With Compact Circularly Polarized Slots in Gap Waveguide for Automotive Radar,’ *IEEE Transactions on Antennas and Propagation*, vol. 72, no. 7, pp. 5578–5588, Jul. 2024, DOI: [10.1109/TAP.2024.3405172](https://doi.org/10.1109/TAP.2024.3405172)
- [17] A. Tinti, S. T. Alfageme, S. D. Biarge and N. Pohl, ‘ $\pm 45^\circ$  Linearly Polarized PCB Antennas for Polarimetric Automotive Radar,’ in *2023 Photonics & Electromagnetics Research Symposium (PIERS)*, Jul. 2023, pp. 571–577, DOI: [10.1109/PIERS59004.2023.10221254](https://doi.org/10.1109/PIERS59004.2023.10221254)
- [18] J. Sun, L. Wu, R. Li, X. Zhang and Y. Cui, ‘A Wideband Cavity-Slotted Waveguide Antenna for mm-Wave Automotive Radar Sensors,’ *IEEE Antennas and Wireless Propagation Letters*, vol. 23, no. 12, pp. 4758–4762, Dec. 2024, DOI: [10.1109/LAWP.2024.3470126](https://doi.org/10.1109/LAWP.2024.3470126)
- [19] W. Li, X. Tang and Y. Yang, ‘Design and Implementation of SIW Cavity-Backed Dual-Polarization Antenna Array With Dual High-Order Modes,’ *IEEE Transactions on Antennas and Propagation*, vol. 67, no. 7, pp. 4889–4894, Jul. 2019, DOI: [10.1109/TAP.2019.2912451](https://doi.org/10.1109/TAP.2019.2912451)
- [20] R. Ferreira, J. Joubert and J. W. Odendaal, ‘A Compact Dual-Circularly Polarized Cavity-Backed Ring-Slot Antenna,’ *IEEE Transactions on Antennas and Propagation*, vol. 65, no. 1, pp. 364–368, Jan. 2017, DOI: [10.1109/TAP.2016.2623654](https://doi.org/10.1109/TAP.2016.2623654)
- [21] O. Khan, J. Meyer, K. Baur and C. Waldschmidt, ‘Hybrid Thin Film Antenna for Automotive Radar at 79 GHz,’ *IEEE Transactions on Antennas and Propagation*, vol. 65, no. 10, pp. 5076–5085, Oct. 2017, DOI: [10.1109/TAP.2017.2741024](https://doi.org/10.1109/TAP.2017.2741024)
- [22] H. Saeidi-Manesh and G. Zhang, ‘Low Cross-Polarization, High-Isolation Microstrip Patch Antenna Array for Multi-Mission Applications,’ *IEEE Access*, vol. 7, pp. 5026–5033, 2019, DOI: [10.1109/ACCESS.2018.2889599](https://doi.org/10.1109/ACCESS.2018.2889599)
- [23] P.-S. Kildal, A. Zaman, E. Rajo-Iglesias, E. Alfonso and A. Valero-Nogueira, ‘Design and experimental verification of ridge gap waveguide in bed of nails for parallel-plate mode suppression,’ *IET Microwaves, Antennas & Propagation*, vol. 5, no. 3, pp. 262–270, 21st Feb. 2011, DOI: [10.1049/iet-map.2010.0089](https://doi.org/10.1049/iet-map.2010.0089)
- [24] C. Bencivenni, A. Haddadi, A. Vosoogh and S. Carlsson, ‘High-Volume Manufacturing of Metallized Plastic Gapwaves Antennas for mmWave Applications,’ in *2023 17th European Conference on Antennas and Propagation (EuCAP)*, Mar. 2023, pp. 1–4, DOI: [10.23919/EuCAP57121.2023.10133066](https://doi.org/10.23919/EuCAP57121.2023.10133066)
- [25] W. Y. Yong, A. Vosoogh, A. Bagheri, C. Van De Ven, A. Hadaddi and A. A. Glazunov, ‘An Overview of Recent Development of the Gap-Waveguide Technology for mmWave and Sub-THz Applications,’ *IEEE Access*, vol. 11, pp. 69 378–69 400, 2023, DOI: [10.1109/ACCESS.2023.3293739](https://doi.org/10.1109/ACCESS.2023.3293739)
- [26] U. Huegel, A. Garcia-Tejero, R. Glogowski, E. Willmann, M. Pieper and F. Merli, ‘3D Waveguide Metallized Plastic Antennas Aim to Revolutionize Automotive Radar,’ *Microwave Journal, International ed.*, vol. 65, no. 9, pp. 32, 34, 36, 38, 40, 42, 44, 46, 48, Sep. 2022, [Online]. Available: <https://www.proquest.com/docview/2716577264/abstract/B934D9D344644998PQ/1>

- [27] S. Trummer, G. F. Hamberger, R. Koerber, U. Siart and T. F. Eibert, ‘Performance analysis of 79 GHz polarimetric radar sensors for autonomous driving,’ in *2017 European Radar Conference (EURAD)*, Oct. 2017, pp. 41–44, DOI: [10.23919/EURAD.2017.8249142](https://doi.org/10.23919/EURAD.2017.8249142)
- [28] A. Kishk, ‘Wide-band truncated tetrahedron dielectric resonator antenna excited by a coaxial probe,’ *IEEE Transactions on Antennas and Propagation*, vol. 51, no. 10, pp. 2913–2917, Oct. 2003, DOI: [10.1109/TAP.2003.816300](https://doi.org/10.1109/TAP.2003.816300)
- [29] H. U. R. Mohammed, ‘Advancements in mmWave Technology: Launch on Package for Automotive Radars,’ 2024.
- [30] J. C. Dash, D. Sarkar and Y. Antar, ‘Design of Series-fed Patch Array with Modified Binomial Coefficients for MIMO Radar Application,’ in *2021 IEEE International Symposium on Antennas and Propagation and USNC-URSI Radio Science Meeting (APS/URSI)*, Dec. 2021, pp. 1027–1028, DOI: [10.1109/APS/URSI47566.2021.9704636](https://doi.org/10.1109/APS/URSI47566.2021.9704636)
- [31] K. Baur, M. Mayer, S. Lutz and T. Walter, ‘77 GHz automotive radar sensors: Antenna concept for angular measurements in azimuth and elevation,’ in *2013 IEEE Radio and Wireless Symposium*, Jan. 2013, pp. 100–102, DOI: [10.1109/RWS.2013.6486654](https://doi.org/10.1109/RWS.2013.6486654)
- [32] G. F. Hamberger, S. Späth, U. Siart and T. F. Eibert, ‘A Mixed Circular/Linear Dual-Polarized Phased Array Concept for Automotive Radar—Planar Antenna Designs and System Evaluation at 78 GHz,’ *IEEE Transactions on Antennas and Propagation*, vol. 67, no. 3, pp. 1562–1572, Mar. 2019, DOI: [10.1109/TAP.2018.2883640](https://doi.org/10.1109/TAP.2018.2883640)
- [33] J. Puskely, T. Mikulasek, Y. Aslan, A. Roederer and A. Yarovoy, ‘5G SIW-Based Phased Antenna Array With Cosecant-Squared Shaped Pattern,’ *IEEE Transactions on Antennas and Propagation*, vol. 70, no. 1, pp. 250–259, Jan. 2022, DOI: [10.1109/TAP.2021.3098577](https://doi.org/10.1109/TAP.2021.3098577)
- [34] K. Anim, J.-N. Lee and Y.-B. Jung, ‘High-Gain Millimeter-Wave Patch Array Antenna for Unmanned Aerial Vehicle Application,’ *Sensors*, vol. 21, no. 11, p. 3914, Jan. 2021, DOI: [10.3390/s21113914](https://doi.org/10.3390/s21113914)
- [35] F. Karami, H. Boutayeb, A. Amn-e-Elahi, A. Ghayekhloo and L. Talbi, ‘Developing Broadband Microstrip Patch Antennas Fed by SIW Feeding Network for Spatially Low Cross-Polarization Situation,’ *Sensors*, vol. 22, no. 9, p. 3268, Jan. 2022, DOI: [10.3390/s22093268](https://doi.org/10.3390/s22093268)
- [36] M. Salucci et al., ‘Spline-Shaped Microstrip Edge-Fed Antenna for 77 GHz Automotive Radar Systems,’ *IEEE Access*, vol. 12, pp. 2086–2099, 2024, DOI: [10.1109/ACCESS.2023.3348240](https://doi.org/10.1109/ACCESS.2023.3348240)
- [37] S. P. Hehenberger, A. Yarovoy and A. Stelzer, ‘A 77-GHz FMCW MIMO Radar Employing a Non-Uniform 2D Antenna Array and Substrate Integrated Waveguides,’ in *2020 IEEE MTT-S International Conference on Microwaves for Intelligent Mobility (ICMIM)*, Nov. 2020, pp. 1–4, DOI: [10.1109/ICMIM48759.2020.9299059](https://doi.org/10.1109/ICMIM48759.2020.9299059)
- [38] F. Bauer and W. Menzel, ‘A 79-GHz Resonant Laminated Waveguide Slotted Array Antenna Using Novel Shaped Slots in LTCC,’ *IEEE Antennas and Wireless Propagation Letters*, vol. 12, pp. 296–299, 2013, DOI: [10.1109/LAWP.2013.2248694](https://doi.org/10.1109/LAWP.2013.2248694)
- [39] M. Mosalanejad, I. Ocket, C. Soens and G. A. E. Vandenbosch, ‘Multi-Layer PCB Bow-Tie Antenna Array for (77–81) GHz Radar Applications,’ *IEEE Transactions on Antennas and Propagation*, vol. 68, no. 3, pp. 2379–2386, Mar. 2020, DOI: [10.1109/TAP.2019.2949723](https://doi.org/10.1109/TAP.2019.2949723)
- [40] Q. Yang et al., ‘Millimeter-Wave Dual-Polarized Differentially Fed 2-D Multibeam Patch Antenna Array,’ *IEEE Transactions on Antennas and Propagation*, vol. 68, no. 10, pp. 7007–7016, Oct. 2020, DOI: [10.1109/TAP.2020.2992896](https://doi.org/10.1109/TAP.2020.2992896)
- [41] P. Zhao, N. Li, Y. Zhang and N. Hu, ‘An SIW Quasi-Pyramid Horn Antenna Based on Patch Coupling Feed for Automotive Radar Sensors,’ *Remote Sensing*, vol. 16, no. 4, p. 692, Jan. 2024, DOI: [10.3390/rs16040692](https://doi.org/10.3390/rs16040692)

- [42] Y.-X. Guo and K.-M. Luk, ‘Dual-polarized dielectric resonator antennas,’ *IEEE Transactions on Antennas and Propagation*, vol. 51, no. 5, pp. 1120–1124, May 2003, DOI: [10.1109/TAP.2003.811486](https://doi.org/10.1109/TAP.2003.811486)
- [43] H. Aliakbari, M. Mosalanejad, C. Soens, G. A. E. Vandenbosch and B. K. Lau, ‘79 GHz Multilayer Series-Fed Patch Antenna Array With Stacked Micro-Via Loading,’ *IEEE Antennas and Wireless Propagation Letters*, vol. 21, no. 10, pp. 1990–1994, Oct. 2022, DOI: [10.1109/LAWP.2022.3187764](https://doi.org/10.1109/LAWP.2022.3187764)
- [44] L. Schulwitz and A. Mortazawi, ‘Millimeter-Wave Dual Polarized L-Shaped Horn Antenna for Wide-Angle Phased Arrays,’ *IEEE Transactions on Antennas and Propagation*, vol. 54, no. 9, pp. 2663–2668, Sep. 2006, DOI: [10.1109/TAP.2006.880761](https://doi.org/10.1109/TAP.2006.880761)
- [45] Q. Ren et al., ‘An Automotive Polarimetric Radar Sensor With Circular Polarization Based on Gapwaveguide Technology,’ *IEEE Transactions on Microwave Theory and Techniques*, vol. 72, no. 6, pp. 3759–3771, Jun. 2024, DOI: [10.1109/TMTT.2023.3329246](https://doi.org/10.1109/TMTT.2023.3329246)
- [46] W. Hartner et al., ‘Reliability and Performance of Wafer Level Fan Out Package for Automotive Radar,’ in *2019 International Wafer Level Packaging Conference (IW LPC)*, Oct. 2019, pp. 1–11, DOI: [10.23919/IW LPC.2019.8914100](https://doi.org/10.23919/IW LPC.2019.8914100)
- [47] B. T. Arnold and M. A. Jensen, ‘The Effect of Antenna Mutual Coupling on MIMO Radar System Performance,’ *IEEE Transactions on Antennas and Propagation*, vol. 67, no. 3, pp. 1410–1416, Mar. 2019, DOI: [10.1109/TAP.2018.2888702](https://doi.org/10.1109/TAP.2018.2888702)
- [48] Q. Ren et al., ‘Gapwaveguide Automotive Imaging Radar Antenna With Launcher in Package Technology,’ *IEEE Access*, vol. 11, pp. 37483–37493, 2023, DOI: [10.1109/ACCESS.2023.3266958](https://doi.org/10.1109/ACCESS.2023.3266958)
- [49] Y. Li and K.-M. Luk, ‘60-GHz Dual-Polarized Two-Dimensional Switch-Beam Wideband Antenna Array of Aperture-Coupled Magneto-Electric Dipoles,’ *IEEE Transactions on Antennas and Propagation*, vol. 64, no. 2, pp. 554–563, Feb. 2016, DOI: [10.1109/TAP.2015.2507170](https://doi.org/10.1109/TAP.2015.2507170)
- [50] I. Mohamed, M. Abdalla and A. E.-A. Mitkees, ‘Perfect isolation performance among two-element MIMO antennas,’ *AEU - International Journal of Electronics and Communications*, vol. 107, pp. 21–31, 1st Jul. 2019, DOI: [10.1016/j.aeue.2019.05.014](https://doi.org/10.1016/j.aeue.2019.05.014)
- [51] H. Cho, J.-H. Lee, S. Kim, J.-W. Yu and B. Ahn, ‘Series-Fed Integrated Lens Antenna for High Gain in Millimeter-Wave Band,’ *IEEE Antennas and Wireless Propagation Letters*, vol. 23, no. 5, pp. 1578–1582, May 2024, DOI: [10.1109/LAWP.2024.3363182](https://doi.org/10.1109/LAWP.2024.3363182)
- [52] Texas Instruments, *Aurrx cascaded radar rf evaluation module (mmwcas-rf-evm) user’s guide*, Rev. SWRU553A, Texas Instruments, Dallas, TX, USA, Feb. 2020, [Online]. Available: <https://www.ti.com/lit/ug/swru553a/swru553a.pdf>
- [53] *Aur2944 evaluation module user’s guide, rev. c*, Literature Number SPRUJ22C, Texas Instruments, Dallas, TX, USA, Sep. 2024, [Online]. Available: <https://www.ti.com/lit/ug/spruj22c/spruj22c.pdf>
- [54] D. Bliss and K. Forsythe, ‘Multiple-input multiple-output (MIMO) radar and imaging: Degrees of freedom and resolution,’ in *The Thirti-Seventh Asilomar Conference on Signals, Systems & Computers, 2003*, vol. 1, Nov. 2003, 54–59 Vol.1, DOI: [10.1109/ACSSC.2003.1291865](https://doi.org/10.1109/ACSSC.2003.1291865)
- [55] K. Forsythe, D. Bliss and G. Fawcett, ‘Multiple-input multiple-output (MIMO) radar: Performance issues,’ in *Conference Record of the Thirty-Eighth Asilomar Conference on Signals, Systems and Computers, 2004.*, vol. 1, Nov. 2004, 310–315 Vol.1, DOI: [10.1109/ACSSC.2004.1399143](https://doi.org/10.1109/ACSSC.2004.1399143)

- [56] E. Fishler, A. Haimovich, R. Blum, D. Chizhik, L. Cimini and R. Valenzuela, ‘MIMO radar: An idea whose time has come,’ in *Proceedings of the 2004 IEEE Radar Conference*, Apr. 2004, pp. 71–78, DOI: [10.1109/NRC.2004.1316398](https://doi.org/10.1109/NRC.2004.1316398)
- [57] E. Fishler, A. Haimovich, R. Blum, L. Cimini, D. Chizhik and R. Valenzuela, ‘Spatial Diversity in Radars—Models and Detection Performance,’ *IEEE Transactions on Signal Processing*, vol. 54, no. 3, pp. 823–838, Mar. 2006, DOI: [10.1109/TSP.2005.862813](https://doi.org/10.1109/TSP.2005.862813)
- [58] V. S. Chernyak, ‘On the concept of MIMO radar,’ in *2010 IEEE Radar Conference*, May 2010, pp. 327–332, DOI: [10.1109/RADAR.2010.5494601](https://doi.org/10.1109/RADAR.2010.5494601)
- [59] M. A. S. Holder and M. Eberspächer, ‘Systematic methods for the synthesis of equidistant MIMO arrays,’ *Advances in Radio Science*, vol. 21, pp. 15–23, 2023, DOI: [10.5194/ars-21-15-2023](https://doi.org/10.5194/ars-21-15-2023)
- [60] L. Xu and J. Li, ‘Iterative Generalized-Likelihood Ratio Test for MIMO Radar,’ *IEEE Transactions on Signal Processing*, vol. 55, no. 6, pp. 2375–2385, Jun. 2007, DOI: [10.1109/TSP.2007.893937](https://doi.org/10.1109/TSP.2007.893937)
- [61] C. Liang et al., ‘Cooperative Automotive Radars with Multi-Aperture Multiplexing MIMO Sparse Array Design,’ *Electronics*, vol. 11, no. 8, p. 1198, Jan. 2022, DOI: [10.3390/electronics11081198](https://doi.org/10.3390/electronics11081198)
- [62] A. Hassani and S. A. Vorobyov, ‘Phased-MIMO Radar: A Tradeoff Between Phased-Array and MIMO Radars,’ *IEEE Transactions on Signal Processing*, vol. 58, no. 6, pp. 3137–3151, Jun. 2010, DOI: [10.1109/TSP.2010.2043976](https://doi.org/10.1109/TSP.2010.2043976)
- [63] X. Zhuge and A. G. Yarovoy, ‘Study on Two-Dimensional Sparse MIMO UWB Arrays for High Resolution Near-Field Imaging,’ *IEEE Transactions on Antennas and Propagation*, vol. 60, no. 9, pp. 4173–4182, Sep. 2012, DOI: [10.1109/TAP.2012.2207031](https://doi.org/10.1109/TAP.2012.2207031)
- [64] J. Li, P. Stoica, L. Xu and W. Roberts, ‘On Parameter Identifiability of MIMO Radar,’ *IEEE Signal Processing Letters*, vol. 14, no. 12, pp. 968–971, Dec. 2007, DOI: [10.1109/LSP.2007.905051](https://doi.org/10.1109/LSP.2007.905051)
- [65] J. Li and P. Stoica, ‘MIMO Radar with Colocated Antennas,’ *IEEE Signal Processing Magazine*, vol. 24, no. 5, pp. 106–114, Sep. 2007, DOI: [10.1109/MSP.2007.904812](https://doi.org/10.1109/MSP.2007.904812)
- [66] J. Li and P. Stoica. ‘MIMO Radar Signal Processing | IEEE eBooks | IEEE Xplore,’ Accessed: 14th Oct. 2025. [Online]. Available: <https://ieeexplore-ieee-org.tudelft.idm.oclc.org/book/5236870>
- [67] M. G. Amin, *Sparse Arrays for Radar, Sonar, and Communications*. Hoboken, NJ: John Wiley & Sons, 2024, DOI: [10.1002/9781394191048](https://doi.org/10.1002/9781394191048)
- [68] M. Eric, A. Zejak and M. Obradovic, ‘Ambiguity characterization of arbitrary antenna array: Type I ambiguity,’ in *1998 IEEE 5th International Symposium on Spread Spectrum Techniques and Applications - Proceedings. Spread Technology to Africa (Cat. No.98TH8333)*, vol. 2, Sep. 1998, 399–403 vol.2, DOI: [10.1109/ISSSTA.1998.723814](https://doi.org/10.1109/ISSSTA.1998.723814)
- [69] M. Huan, J. Liang, Y. Wu, Y. Li and W. Liu, ‘SASA: Super-Resolution and Ambiguity-Free Sparse Array Geometry Optimization With Aperture Size Constraints for MIMO Radar,’ *IEEE Transactions on Antennas and Propagation*, vol. 71, no. 6, pp. 4941–4954, Jun. 2023, DOI: [10.1109/TAP.2023.3262157](https://doi.org/10.1109/TAP.2023.3262157)